

OPEN ACCESS

Repository of the Max Delbrück Center for Molecular Medicine (MDC) in the Helmholtz Association

<https://edoc.mdc-berlin.de/19973/>

Ophthalmic magnetic resonance imaging: where are we (heading to)?

Niendorf T., Beenakker J.W.M., Langner S., Erb-Eigner K., Bach Cuadra M., Beller E., Millward J.M., Niendorf T.M., Stachs O.

This is an Accepted Manuscript of an article published by Taylor & Francis in *Current Eye Research* on 04/02/2021, available online at
<http://www.tandfonline.com/doi/full/10.1080/02713683.2021.1874021>.

The original article has been published in final edited form in:

Current Eye Research
2021 SEP 02 ; 46(9): 1251-1270
2021 FEB 04 (first published online: final publication)
doi: [10.1080/02713683.2021.1874021](https://doi.org/10.1080/02713683.2021.1874021)

Publisher: [Taylor & Francis](https://www.tandfonline.com)

Copyright © 2021 Taylor & Francis Group, LLC.

Ophthalmic Magnetic Resonance Imaging: Where Are We (Heading To)?

Thoralf Niendorf^{1,2}, Jan-Willem M. Beenakker³, Sönke Langner⁴, Katharina Erb-Eigner⁵,
Meritxell Bach Cuadra⁶, Ebba Beller⁴, Jason M. Millward¹, Thea Marie Niendorf⁷ and
Oliver Stachs^{8,9}

¹ Berlin Ultrahigh Field Facility, Max Delbrueck Center for Molecular Medicine in the Helmholtz Association,
Berlin, Germany

² MRI.TOOLS GmbH, Berlin, Germany

³ Department of Ophthalmology and Department of Radiology, Leiden University Medical Centre, Leiden, the
Netherlands

⁴ Institute of Diagnostic and Interventional Radiology, Rostock University Medical Center, Rostock, Germany

⁵ Department of Radiology, Charité - Universitätsmedizin Berlin, corporate member of Freie Universität Berlin,
Humboldt-Universität zu Berlin, and Berlin Institute of Health, Berlin, Germany.

⁶ Center for Biomedical Imaging (CIBM), Department of Radiology, Lausanne University and University Hospital,
Lausanne, Switzerland

⁷ Rostock University Medical Center, Rostock, Germany.

⁸ Department of Ophthalmology, Rostock University Medical Center, Rostock, Germany.

⁹ Department Life, Light & Matter, University Rostock, Rostock, Germany.

Abstract

Magnetic resonance imaging of the eye and orbit (MR eye) is a cross-domain research field, combining (bio)physics, (bio)engineering, physiology, data sciences and ophthalmology. A growing number of reports document technical innovations of MR eye and promote their application in preclinical research and clinical science. Realizing the progress and promises, this review outlines current trends in MR eye. Examples of MR eye strategies and their clinical relevance are demonstrated. Frontier applications in ocular oncology, refractive surgery, ocular muscle disorders and orbital inflammation are presented and their implications for explorations into ophthalmic diseases are provided. Substantial progress in anatomically detailed, high-spatial resolution MR eye of the eye, orbit and optic nerve is demonstrated. Recent developments in MR eye of ocular tumors are explored, and its value for personalized eye models derived from machine learning in the treatment planning of uveal melanoma and evaluation of retinoblastoma is highlighted. The potential of MR eye for monitoring drug distribution and for improving treatment management and the assessment of individual responses is discussed. To open a window into the eye and into (patho)physiological processes that in the past have been largely inaccessible, advances in MR eye at ultrahigh magnetic field strengths are discussed. A concluding section ventures a glance beyond the horizon and explores future directions of MR eye across multiple scales, including in vivo electrolyte mapping of sodium and other nuclei. This review underscores the need for the (bio)medical imaging and ophthalmic communities to expand efforts to find solutions to the remaining unsolved problems and technical obstacles of MR eye, with the objective to transfer methodological advancements driven by MR physics into genuine clinical value.

Keywords

Ophthalmology, eye, orbit, imaging, Magnetic Resonance Imaging

Introduction

The demand for new strategies for early detection and treatment of ocular diseases requires that we deepen our understanding of the underlying pathophysiological processes and molecular mechanisms, which in turn calls for new ways to visualize the eye and the orbit and to image ocular disease states at multiple scales of length and time. Magnetic resonance imaging (MRI) of the eye and orbit (hereafter referred to as 'MReye'¹⁻⁵) as well as the spatial arrangements of the eye segments and their masses, is increasingly being used in basic and translational research, and clinical diagnostics.

Although the ophthalmic clinic is generally equipped with a wide variety of imaging modalities including fundus photography, optical coherence tomography and ultrasound, MReye can complement these tools, and address a number of their limitations. Crucially, most ophthalmic imaging modalities use optical techniques and are therefore limited to imaging transparent tissues. MReye allows the characterization of opaque tissues, such as intra-ocular tumors. Optical images are distorted as light is refracted by the cornea and lens, which constitutes a challenge for radiotherapy planning. Unlike optical approaches, MRI can image orbital structures behind the globe, such as the eye muscles, which otherwise can only be indirectly evaluated, for example using the clinical activity scale in Graves' Orbitopathy. MReye provides 3D volumetric imaging, whereas conventional techniques such as fundoscopy are constrained to 2D cross-sections of the eye. MReye has also enabled the quantification and mapping of parameters related to biophysics and physiology such as perfusion of intra-ocular lesions, water diffusion in uveal melanoma, and assessment of sodium content. This opens up an entirely new arena for the diagnosis of ocular lesions, which so far has primarily been based on purely descriptive assessments. With a spatial resolution close to that of computed tomography (CT), MRI can serve as a diagnostic tool for a wide range of ocular diseases including eye tumors and optic neuropathies. Ultimately, the development of ocular MRI applications aims towards image-based biometry. MReye also has a role to play in screening for ophthalmic disease, teaching, clinical trials and in virtual ophthalmology and telemedicine.

This review surveys the state-of-the-art of MReye and highlights cutting-edge technologies. Examples of novel MReye strategies and emerging applications are presented, with demonstrations of their clinical relevance, together with a perspective into future directions.

MReye in ocular oncology, refractive surgery, ocular muscle disorders and orbital inflammation

MReye for ocular oncology

1
2
3 Uveal Melanoma (UM) is the most common primary eye tumor. Its distant metastases render it one
4 of the very few life threatening ocular conditions⁶. Conventionally, UM is diagnosed using fundus
5 photography, fluorescence angiography and ultrasound (US). The optimal treatment approach for
6 UM depends primarily on its size and location. Small UM, e.g. less than 8mm thickness, are generally
7 treated with local brachytherapy, whereas larger UM generally receive external beam therapy, such
8 as Proton Therapy (PT), or may require enucleation^{7,8}. In ophthalmic US the observed tumor
9 thickness depends heavily on the orientation of the US transducer. This thickness is often
10 overestimated as the transducer cuts obliquely through the tumor⁹. US is constrained by the modest
11 contrast between tumor and sclera, and therefore has a relatively high inter-observer variation of
12 0.6 mm¹⁰. MReye can image the tumor with superior tissue contrast (Figure 1), thus providing a
13 more accurate and reproducible evaluation of the tumor dimensions. Incorporating MReye into
14 clinical practice has proven to be cost-effective for patients with medium-size UM, as the avoidance
15 of tumour size overestimation using three-dimensional (3D) MR-based measurements generally
16 results in smaller volumes, making at least 10% of these patients eligible for brachytherapy instead
17 of the more invasive and expensive PT, or enucleation, which would otherwise have been
18 prescribed.¹¹

19
20
21
22
23
24
25
26
27
28
29
30
31
32
33
34
35
36
37
38
39
40
41
42
43
44
45
46
47
48
49
50
51
52
53
54
55
56
57
58
59
60
3D MR-based visualization of the tumor is also beneficial for radiotherapy planning for UM.
Several studies report developments in MR-based PT planning, which can not only incorporate the
3D shape of the tumor, but also the actual location of the organs-at-risk^{4,11-13}. MR-based treatment
and position verification methods are developed for brachytherapy planning of ocular tumors,
enabling treatment planning based on the unique tumor geometry and plaque location of the
individual patient (Figure 2).¹⁴ These advances in ocular radiotherapy have been facilitated by the
demonstration of the MR-safety of tantalum markers used in PT-planning,¹⁵ and the confirmation of
geometric stability of the eye and tumor, between MR-images acquired in a supine position and the
delivery of PT in a sitting position.¹⁶

MR-based eye models for refractive surgery

Efforts in refractive surgery have expanded from central vision to include peripheral vision.
In cataract surgery, a decrease in peripheral image quality was observed after implantation of an
intra-ocular lens.¹⁷ Furthermore, studies on the development of myopia in children suggest a link
between peripheral refraction and a gradual elongation of the eye.^{18,19} Since peripheral refraction is
partly related to the retinal shape,²⁰ various approaches have been explored to accurately measure
the eye shape, and MReye has become instrumental for this (Figure 2). MRI revealed a less oblate
shape in myopic eyes as compared to emmetropic eyes.²¹⁻²³ The increased spatial resolution

1
2
3 available at ultrahigh magnetic field strengths has facilitated quantification of small changes in lens
4 shape with increasing age,²⁴ and has revealed submillimeter irregularities that could have an
5 important influence on the subjects' peripheral vision.²⁵ More recently, high-resolution MR eye
6 techniques have been applied in clinical studies, for example to assess the geometric relation
7 between the iris and intra-ocular lens in patients with Negative Dysphotopsia.²⁶
8
9
10
11
12

13 ***MR eye of orbital inflammation***

14
15 MRI is the modality of choice for the evaluation of orbital inflammation, because of its
16 superior soft tissue contrast and spatial resolution.²⁷ T₁- and T₂-weighted MRI are instrumental for
17 tissue characterization, and can help to determine the extent of inflammation in orbital structures.
18 In T₁-weighted images inflammatory lesions are hypointense to isointense. For T₂-weighted MRI the
19 signal intensity of inflammatory lesions is governed by the balance between edema, which appears
20 hyper-intense, and fibrosis, which appears hypo-intense. Incorporating fat suppression into T₂-
21 weighted MRI makes edema even more conspicuous. MR eye of optic nerve inflammation appears
22 hyperintense on T₂-weighted images, together with unilateral optic nerve swelling in the
23 retrobulbar/intra-orbital segment²⁸.
24
25
26
27
28
29

30
31 In addition to T₁- and T₂-weighted imaging, parametric mapping using quantitative MR-
32 techniques has the potential to provide even greater impact for the assessment of ocular
33 inflammation. In quantitative MRI, the effects of specific biological parameters can be probed, such
34 as the tissue water content, water diffusion, perfusion and lesion vascularity. These biomarkers are
35 routinely used in a wide range of applications, and have become increasingly available for
36 MR eye^{29,30}. For example, diffusion weighted imaging (DWI) probes the diffusion of water on a
37 microscopic level (Figure 3) and holds the potential for enhancing diagnostic accuracy compared to
38 morphological techniques. DWI was shown to differentiate orbital inflammatory processes from
39 malignant lesions³¹. Combining DWI with morphological MRI can help to reveal the underlying
40 causes of inflammatory disorders.¹⁸ Without MRI, these assessments can often only be performed
41 with biopsy when these pathologies are located behind the globe, and are therefore not accessible
42 to optical methods. Combining morphological MRI and mapping of the apparent water diffusion
43 coefficient (ADC) has value for the differential diagnosis of orbital lymphoma and idiopathic orbital
44 inflammatory pseudotumors³². The ADC was shown to be higher in inflammatory and benign lesions
45 as compared to malignant lesions, resulting from an increased intracellular fraction of water rather
46 than cellular infiltration³³. To advance this approach, DWI has been specifically tailored for the eye,
47 to enable higher precision images free from geometric distortion³⁴. Other examples of quantitative
48 MRI include mapping of the spin-spin relaxation time (T₂) and fat-water imaging (Figure 3) using
49
50
51
52
53
54
55
56
57
58
59
60

1
2
3 Dixon techniques to quantify the amount of inflammation and fatty infiltration of muscles. These
4 techniques have been translated to ophthalmic applications, providing detailed, noninvasive
5 assessment of the extra-ocular muscles in Graves' orbitopathy and Myasthenia gravis.^{35,36}
6
7
8
9

10 **MReye: the intersection between ophthalmology and radiology**

11
12 Technical progress has continuously improved MRI quality of the eye and orbital cavity^{1,37-40}.
13 Due to the superior soft tissue contrast and the lack of ionizing radiation, MRI provides an attractive
14 alternative to CT for the diagnosis of diseases of the eye and orbit. These diagnostic possibilities
15 have become ever more diverse, and the range of clinical indications has broadened considerably⁴¹.
16 The main indications for MReye currently include ambiguous ophthalmoscopic findings such as
17 vitreous opacification, bleeding and retinal detachment, local staging of ocular mass lesions (e.g.
18 uveal melanoma, retinoblastoma) as well as planning for their treatment, and the assessment of
19 injuries involving non-metallic foreign bodies. A recent addition to these indications are masses
20 within the eye lid. Unlike with conventional ophthalmic techniques, MReye could identify which
21 eyelid layers are affected, thus enabling more conservative surgery in a subset of patients.⁴²
22 Indications for MReye of structures behind the globe and in the deeper orbital cavity include unclear
23 protrusion of the globe, as well as staging of mass lesions with regard to dignity and entity. UM is
24 often complicated by exudative retinal detachment, which is sometimes mistaken for a
25 rhegmatogenous detachment and subsequently treated with vitrectomy with silicone oil (SiOil)
26 tamponade. The latter is challenging if not impossible to image with US. MReye enables high-
27 resolution imaging of vitrectomized eyes with SiOil tamponade, facilitating treatment planning and
28 follow-up in UM patients.⁴³ MRI of the orbital cavity is warranted in clinically unclear situations of
29 thyroid associated orbitopathy such as unilateral involvement, missing thyroid disease and
30 assessment of disease activity⁴⁴.
31
32
33
34
35
36
37
38
39
40
41
42
43

44 Using MReye to achieve the correct diagnosis is crucial, since tissue sampling and surgery in
45 the orbital cavity especially behind the globe, is technically difficult and may be associated with
46 adverse outcomes. Nevertheless, imaging of the eye and orbit can be challenging. Involuntary
47 movements of the eye can have a significant impact on image quality. Artifacts induced by magnetic
48 field inhomogeneities can occur due to the adjacent air-containing paranasal sinuses and maxillary
49 sinuses. The radiologist or interpreting physician must be experienced with assessing these artifacts
50 since they can mimic disease indications such as orbital inflammation, especially around the orbital
51 floor.
52
53
54
55
56

57 MRI scans of a metallic intraocular foreign body are very rare, primarily due to the magnetic
58 susceptibility and resultant tissue damage, making the procedure contraindicated. The initial
59
60

1
2
3 imaging modality of choice for diagnostic evaluation of a suspected intraorbital foreign bodies is a CT
4 scan. MR eye is generally contraindicated as first-line imaging because the strong magnetic field may
5 dislodge metallic intraocular foreign, potentially causing damage to ocular structures or even
6 blindness.
7
8
9

10 The advent of multiparametric imaging adds functional information to standard anatomical
11 T_1 - and T_2 -weighted imaging protocols, enhancing diagnostic possibilities in the eye and orbit ⁴⁵.
12 Being able to differentiate between benign and malignant lesions in the orbital cavity has a major
13 impact for the patient, by avoiding tissue sampling and surgery as much as possible. DWI has great
14 value in classifying unclear orbital lesions ^{17,46-52}. An average ADC of $0.9 \times 10^{-3} \text{ mm}^2/\text{s}$ was reported
15 for malignant lesions ¹⁷. For benign orbital lesions, an average ADC of $1.43 \times 10^{-3} \text{ mm}^2/\text{s}$ was
16 reported ¹⁷. Consequently, a model containing two ADC thresholds was proposed to classify orbital
17 lesions into 'malignant', 'benign' and 'undetermined'. With this progress DWI has proven its value for
18 the differentiation of UM from benign lesions, and has shown strong potential as an early biomarker
19 of radiotherapy response.^{17,27,53,54} Figure 4 shows an example of two patients with similar signal
20 characteristics in the T_1 - and T_2 -weighted images but with different signal characteristics for DWI.
21 The development of distortion-free DWI has been very useful in the assessment of orbital
22 pathologies, especially when the anatomical structures are small ⁵⁵. Figure 4 depicts optic nerve
23 ischemia using distortion-free DWI.
24
25
26
27
28
29
30
31
32

33 Recent studies have shown the diagnostic advantages of perfusion weighted imaging (PWI)
34 ⁵⁶⁻⁵⁹. The time course of the dynamic contrast-enhanced MR signal allows conclusions to be drawn
35 about the vascularization and the microcirculation of different lesions (Figure 3). PWI helps to
36 classify mass lesions into 'benign' and 'malignant'. Benign mass lesions tend to show a slow increase
37 in signal intensity over time, whereas malignant lesions typically show a fast increase of signal
38 intensity, and after reaching a peak, a plateau or even a drop in signal intensity occurs ('washout
39 phenomenon'). This is particularly useful in distinguishing mass lesions which may have similar signal
40 characteristics in standard T_1 - and T_2 -weighted images. PWI images can provide the radiologist with
41 more confidence in classifying these lesions (Figure 3). In ocular oncology, the visual appearance of
42 the lesion, e.g. pigmented with orange spots, is used to provide a strong indication of the type of
43 lesion (UM in this case).⁶⁰ However, when a lesion is located behind the iris, or covered with blood or
44 liquid, such a visual inspection is not always possible. In these cases, PWI can provide crucial insights
45 into the origin of the lesion. For example, choroidal hemangioma show a significantly stronger
46 enhancement in PWI than UM.⁶¹ Dedicated analysis tools have been developed for PWI of the eyes
47 to correct these images for eye-motion and to incorporate differences in tumor pigmentation in the
48 models used for quantification.
49
50
51
52
53
54
55
56
57
58
59
60

1
2
3 The application of contrast media for (dynamic) contrast enhancement should be used with
4 caution, and the potential benefits and risks must be evaluated individually for every patient. Tissue
5 deposits of gadolinium after the administration of MR contrast agents have become a controversial
6 issue and a serious safety concern, with implications for patient care and clinical use ^{62,63}.
7 Gadolinium retention in the brain was demonstrated, especially in patients who had several contrast
8 media applications ⁶⁴. A recent study showed leakage of gadolinium-based contrast into the anterior
9 chamber of the eye in children shortly after intravenous injection ⁶⁵.

10
11 A systematic approach is required for interpreting MR images, and reports to the referring
12 clinician should include information on location of lesions, adjacent structures, size and
13 characteristics (such as hemorrhage and necrosis) as well as information on lesion dignity (benign
14 versus malignant). Table 1 provides a summary of pathologies encountered in the eye and orbital
15 cavity which warrant high-resolution MR imaging. The most common benign orbital mass lesions are
16 hemangiomas. DWI is particularly helpful in evaluating lacrimal gland lesions. Lymphomas must be
17 accurately discriminated from benign mixed tumors since the latter should not be biopsied due to
18 increased recurrence rates along the biopsy pathway. Lymphomas typically show restricted diffusion
19 whereas benign mixed tumors do not.

30 31 32 **MR eye to monitor drug delivery and ocular pharmacokinetics**

33
34 The eye can be divided into the anterior segment (approximately one third of the eye
35 volume), and the posterior segment (accounting for the remaining two thirds). The choice of drug
36 delivery to the eye mainly depends on the affected area, mode of action and the desired therapeutic
37 effect. The treatment of anterior eye diseases is most commonly performed via topical
38 administration, whereas intravitreal injection is the gold standard for treating posterior eye
39 diseases⁶⁶. Intravitreal injections may have severe side effects including retinal detachment, vitreous
40 hemorrhaging, intraocular inflammation, endophthalmitis or elevated intraocular pressure ⁶⁷.
41 Moreover, poor patient compliance is a crucial problem for intravitreal administration. Drugs
42 delivered to the back of the eye encounter multiple physiological barriers. The vitreous is gel-like,
43 acellular and consists primarily of water with collagen, glycosaminoglycan and hyaluronic acid
44 supporting the structure formation of the vitreous ⁶⁸. In contrast to the vitreous, the retina is a
45 complex collection of tissues consisting of multiple layers of biological barriers including Bruch's
46 membrane, the retinal pigment epithelium, retinal endothelia, inner- and outer-limiting membrane
47 as well as Müller cells. The retinal pigment epithelium is part of the blood-retina barrier, and this
48 structure is a reason why it is difficult to achieve therapeutic levels of drugs in the retina after
49 systemic administration⁶⁹. Nevertheless, retinal degenerative diseases such as age-related macular
50
51
52
53
54
55
56
57
58
59
60

1
2
3 degeneration, diabetic retinopathy and macular edema, can lead to blindness and are increasing due
4 to the aging population⁷⁰. Drug delivery to the posterior eye segment continues to pose a challenge
5 in ophthalmology and has become an important focus for research for pharmaceutical and
6 biotechnology companies. Given the current need for new therapeutic options, suitable imaging
7 tools are necessary for improving disease detection, evaluation and adjustment of treatment
8 protocols in real time. and to help streamline the drug development process ⁷¹. Reliable ocular
9 pharmacokinetic data are needed to ensure successful development of novel ocular drug-delivery
10 methods and improvements of the existing methods ⁷². Patients treated with drugs via intravitreal
11 injections need to visit the ophthalmic clinic very regularly (e.g. every month), which presents a
12 substantial burden for the clinics and the patients. Advanced methods for controlled drug delivery
13 and monitoring would be instrumental to offset this burden for the benefit of patient comfort and
14 cost reduction.

15
16
17
18
19
20
21
22
23
24
25
26
27
28
29
30
31
32
33
34
35
36
37
38
39
40
41
42
43
44
45
46
47
48
49
50
51
52
53
54
55
56
57
58
59
60
Several studies have demonstrated the usefulness of MRI for providing insights into ocular
transport barriers, clearance pathways, penetration routes and aqueous humor dynamics ⁷³⁻⁷⁶.
Moreover, qualitative and quantitative longitudinal evaluations of drug delivery systems have been
performed with MRI, regarding drug location and release kinetics in periocular, intrascleral,
suprachoroidal and intravitreal administration ⁷⁷⁻⁸⁰, the latter also after injection of silicone oil
tamponade agent within vitrectomy surgery ⁸¹. MRI can also be useful in the study of penetration
routes and distribution of ionic permeants in the eye during and after iontophoresis, for constructing
iontophoresis protocols and device testing ^{82,83}. Conventional MRI contrast agents have been widely
used, inter alia, to investigate dysfunction in the blood-retinal barrier function ^{84,85}. Figure 5 shows
contrast distribution in a pig eye ex vivo after subcorneal injection of a gadolinium-based contrast
agent, and after application of 2ml of contrast agent in the anterior chamber.

Dynamic contrast-enhanced PWI is currently commonly used for preclinical and clinical
evaluation of anti-angiogenesis inhibitors ^{86,87}. PWI allows quantitative pharmacokinetic modelling,
which is an additional benefit over qualitative Fluorescence angiography (FAG). Although ocular
applications of PWI are still at an early development stage, preliminary findings are promising. PWI
showed a strong correlation between the transfer constant (K_{trans}) from vascular to extravascular
extracellular space, and tumor genetics^{59,88}. An alternative to traditional PWI is offered by arterial
spin labeling (ASL) techniques, mostly used to measure cerebral blood flow ⁸⁹. ASL has also been
shown to have the potential to monitor and assess retinal pathologies by detecting changes in
retinal and choroidal blood flow ^{90,91}.

Owing to the development of contrast agents tailored for specific objectives, MRI has
evolved into a versatile technique with multiple functions, and has become one of the most

1
2
3 powerful noninvasive imaging tools in the field of molecular imaging (MI). MI integrates biology at
4 the molecular level with in vivo imaging at the cellular and subcellular level. This allows the
5 monitoring and measurement of biological processes in living subjects, thereby providing
6 information similar to that obtainable from biopsy, but noninvasively and performed in real time ⁹².
7
8 Here nanotechnology can serve as an ideal framework for interfacing contrast agents with
9 molecular biomarkers in vivo, since the nanoscale is the scale at which molecular interactions occur
10 ⁷¹. Among the first nanoparticle structures used for MI were superparamagnetic iron oxide
11 nanoparticles ⁹³. Distribution of the nanoparticles in the eye could be tracked in vivo at different
12 time points after intravitreal injection by MRI⁹⁴. Moreover, the nanoparticles can be combined with
13 coating proteins, such as human serum albumin. Human serum albumin bears functional groups
14 (e.g., hydroxyls, amines, carboxylates and thiols), which can be used for conjugation of various
15 biomolecules, and can improve the pharmacokinetics of peptide- or protein-based drugs. Albumin
16 has low toxicity, is readily available, biodegradable (average blood half-life~19 days) and is
17 preferentially uptaken in tumors and inflamed tissues ⁹⁵. For instance, albuminated polylactic-co-
18 glycolic acid nanoparticles of bevacizumab, injected intravitreally in rabbits, were found to prolong
19 the vitreous concentration of bevacizumab and retain the activity, protected against aggregation
20 and instability ⁹⁶.

21
22
23
24
25
26
27
28
29
30
31
32
33
34
35
36
37
38
39
40
41
42
43
44
45
46
47
48
49
Magnetic resonance spectroscopy (MRS) measures chemical shift information of individual
molecules or components of molecules, thereby allowing the study of the biochemistry and
metabolism of disease processes within the subject ⁹⁷. ¹H-MRS assessment of the visual system and
the visual cortex suggest a significant value of this method for uncovering the processes and
mechanisms of developmental and pathophysiological changes systematically along visual pathways
⁹⁸⁻¹⁰¹. Moreover, ¹⁹F-MRS was used to follow the dynamics of a fluorine-containing corticosteroid in
the eye, administered by intravitreal and subconjunctival injections. Notwithstanding the high
specificity of ¹⁹F-MR, the relatively low sensitivity versus conventional assays remains a limitation.
Improving the detection limits so that ¹⁹F-MR may be sensitive enough to evaluate the
pharmacokinetics of ocular drug delivery methods will require further MR hardware improvements
and pulse sequence developments¹⁰².

50
51
52
53
54
55
56
57
58
59
60
MRI allows for the real-time visualization, localization, characterization and quantification of
ophthalmic drugs after their administration, in a safe and non-invasive way. This can help foster the
objective of improving the application and permanence of ophthalmic drugs in their sites of action.
MR eye offers great potential for the development of ophthalmic drugs and delivery systems for
posterior eye diseases.

MR eye microscopy

Unlike common imaging modalities in ophthalmology including Scheimpflug imaging, US, US Biomicroscopy or Optical Coherence Tomography, MR eye affords distortion-free assessment of the orbit, the globe and the optic nerve. MR eye is not subject to operator-dependent error. With MR eye the image quality depends on the magnetic field homogeneity and the sensitivity of the radiofrequency (RF) antennae used for signal detection. Recent advances in MR technology allow ex and in vivo imaging with submillimeter spatial resolution in reasonable imaging time.

MRI of the orbit at 1.5 tesla (T) is well-established using head volume RF coils for signal detection¹⁰³. With the advent of dedicated small RF surface coils^{104,105}, spatial resolution has been significantly increased, allowing differentiation of orbital tumors from subretinal fluid. Increasing the magnetic field strength promotes the signal-to-noise ratio (SNR), the most important determinant of image quality. This boost can be used to reduce scanning time for the benefit of minimizing the impact of bulk eye motion on image quality, or to enhance spatial resolution. With the increasing availability of 3.0 T MR instruments spatial resolution has significantly improved for imaging the eye¹⁰⁶⁻¹⁰⁸ and the optic nerve¹⁰⁹. The value of increasing magnetic field strength even further, and of tailoring RF coil designs to boost SNR and spatial resolution has been demonstrated¹⁰³. These gains allowed quantitative analysis of lesions of the orbit¹¹⁰, the optic nerve¹¹¹ and the eye lid⁴² using DWI and diffusion tensor imaging (DTI).

MR microscopy (MRM) refers to imaging with an in-plane spatial resolution of $\leq 100\mu\text{m}$ ¹¹². MRM enabled differentiation of the choroid, retina and sclera of the human eye *ex vivo* (Figure 6)¹¹³ and supported *ex vivo* studies of the accommodation apparatus¹¹⁴. *Ex vivo* examinations of the human eye at 9.4 T permitted an in-plane spatial resolution of 32-50 μm ^{34,112}. Using a magnetic field strength of 9.4 T in conjunction with a cryogenically cooled RF coil to enhance signal detection affords high resolution *ex vivo* anatomical imaging and DTI of the human optic nerve (Figure 6). MRM can also be used for the evaluation of orbital masses¹¹⁵. Recent work demonstrated the value of preclinical MRM at 9.4 T and at 17.6 T for *ex vivo* evaluation of the extent and microstructural anatomy of retinoblastoma, in comparison with histopathology. This work facilitated visualization of subtle subretinal tumour seeds with a size $< 300\mu\text{m}$.¹¹⁶ Although the spatial resolution of MRM is an order of magnitude inferior to that of conventional histology, the major advantages of MRM are its non-invasiveness, and the ability to acquire images in any arbitrary plane with the possibility of quantitative imaging in vivo. *Ex vivo* MRM of uveal melanomas yielded an excellent correlation of the structural features obtained from imaging (Figure 6) with conventional histology and *in vivo* imaging techniques^{55,117}. MRM is also instrumental for the evaluation of the optic nerve, the central retinal artery that runs in the dura mater of the optic nerve and the extraocular muscles that control

1
2
3 eye motion (Figure 6). Advancements in MRM render this approach an important adjunct for clinical
4 imaging and a vital tool in ophthalmological research.
5
6
7
8
9

10 **Synergy of MReye with image processing and artificial intelligence**

11
12

13 ***Opportunities for discovery***

14
15 In an era of increasing recognition and knowledge of ocular disease, MReye yields new
16 insights at the functional, physio-metabolic, molecular and cellular levels. In order to integrate these
17 findings into a coherent picture of the eye, its tissues and the orbit for early interception of disease
18 and treatment planning, it is becoming increasingly crucial to make use of the tools of data science.
19 For example, access to an on-the-fly direct 3D patient-specific model of the tumor volume and the
20 eye structures remains an unmet clinical need thus far. This clinical need provides a strong
21 motivation for connecting MRI with advanced image processing, visualization algorithms,
22 quantitative analysis, artificial intelligence and predictive analysis with the ultimate goal to translate
23 MReye-guided computer-assisted diagnosis, treatment planning and intervention into the
24 ophthalmic clinic.
25
26
27
28
29
30
31

32 3D imaging is opening up opportunities in the treatment of ocular tumors in children and
33 adults ^{32,91,108,118,119}. MRI with an in-plane spatial resolution of about 0.5-1.0 mm along each direction
34 can clearly identify eye structures. Importantly, this includes the possibility of imaging the freely
35 moving human eye, which makes fixating or administration of paralytics or anaesthetics obsolete,
36 vastly improving patient comfort and compliance ¹²⁰. MRI can readily distinguish between normal
37 anatomy and pathological regions such as the gross tumor volume or retinal detachment.
38 Furthermore, MRI provides valuable information for tumour tissue characterization, for example
39 between enhancing and non-enhancing regions (as in retinoblastoma) or between nodular and
40 diffuse appearance (as in UM). Adding advanced image processing with a strong data science
41 dimension to MReye will expand the field into uncharted territory, with the possibility to generate
42 patient-specific 3D models of the pathological eye, in near real-time and with minimum human
43 assistance.
44
45
46
47
48
49
50
51
52
53

54 ***Automated segmentation of MReye***

55 There is a dearth of approaches for automated segmentation of healthy ocular structures
56 from 3D MRI or CT. Pioneering studies on this topic have reported on performing parametric
57 modeling of the eye using pre-established shapes such as spheres and ellipsoids. EYEPLAN ¹²¹
58
59
60

1
2
3 presented a framework that estimates the shape of the lens, cornea and sclera by combining
4 parametric spheres. Similarly, OCTOPUS ¹¹ reconstructed anatomical eye structures (e.g. lens or
5 vitreous humor (VH)) as combinations of ellipsoids. Both of these methods were semi-automated,
6 requiring an expert to assist with manually pre-selecting measurements and landmarks in order to
7 initialize the respective models. The modeling capabilities of these approaches are limited to a linear
8 eye-growing pattern, dependent on the age of the patient. Following these initial reports more
9 sophisticated image processing techniques have explored more complex models, enabling the
10 segmentation of more regions of interest (ROI) inside the eye. For example, 3D modeling of the eye
11 based on MReye using spherical meshes has been suggested ¹²². This approach leveraged the
12 posterior corneal pole and a sphericity modifying parameter. An atlas-based segmentation algorithm
13 using parametric active contours together with an ellipsoid model has also been proposed. This
14 approach enabled more accurate segmentations of the sclera and the lens¹²³.

15
16
17
18
19
20
21
22
23 The main shortcoming of parametric models is that they rely on strictly pre-defined
24 geometry and lack statistical information (both related to image intensity and shape variations) that
25 could be extracted from the anatomical variability over a given population. To this end, machine
26 learning (ML) based Active Shape modeling (ASM) ¹²⁴ provides a robust solution for deforming the
27 shape of a structure using a constrained statistical model-based segmentation algorithm trained
28 upon a dataset. This development culminated in the first semi-automated method, requiring minor
29 user interaction, to segment the sclera, the cornea and the lens on CT images of adult patients ¹²⁵.
30 This triggered progress on statistical shape models for automated segmentation of the sclera, VH,
31 and the lens using T₁-weighted images of eyes of healthy children, and eyes of children with
32 unilateral or bilateral tumours, obtained at 3.0 T MR (Figure 7) ^{126,127}. This approach was reproduced
33 for segmentation of eyes in awake adults using T₁-weighted images acquired at 1.5T, demonstrating
34 the presence of pronounced motion and bias field artefacts with bigger eye volume versus asleep
35 children ^{128,129}. This work also confirmed the ability to build a 3D UM patient-specific eye model with
36 the presence of tumors and tantalum clips, and confirmed that ASM was able to accurately segment
37 eye structures even in the presence of tumors ^{128,129}. ML-based MReye radiomics analysis represents
38 a promising tool kit for discriminating between UM and other intraocular masses in adults¹³⁰.

39
40
41
42
43
44
45
46
47
48
49
50 Semi-automated eye structure segmentation has been explored for 7.0 T MRI to measure
51 the 3D shape of the retina to study abnormal shape changes and peripheral vision. ^{25,26} Retinal
52 topographic maps were constructed based on the segmentation of the lens and vitreous body
53 utilizing a series of region growing, multiple threshold and connected component steps.

54
55
56
57
58
59
60
Deep learning is an important branch of machine learning and artificial intelligence (AI)¹³¹.
DL holds promise to automatically pinpoint, identify and grade pathological features in ocular

1
2
3 diseases ¹³². A supervised DL algorithm was explored for segmenting sclera, lens and head of the
4 optic nerve (and also the tumor, see section below) in using a 3D-Unet and additional post-
5 processing steps ¹²⁸. This potential invites ophthalmology to embrace the application of DL with
6 MReye.
7
8
9

10 11 ***Automated ocular tumor segmentation*** 12

13 Few studies have explored automated segmentation of ocular tumors with MRI thus far.
14 Initial methods were developed for segmentation of retinoblastoma (RB) in children. A 3D
15 convolutional neural network (CNN) tailored for RB segmentation was reported using multi-spectral
16 MRI sequences and patient-specific features extracted from initial ASM segmentation in 16 patients
17 ^{126,133}. Another deep learning method based on a 3D U-net architecture was employed for
18 segmentation in 32 patients with RB ¹²⁸. In addition to the patient data, healthy adults and children
19 were included in the training data. This approach aimed at solving the dual problem of identifying
20 eye structures and tumor segmentation simultaneously. RB segmentation was also presented in 24
21 patients using a combination of ASM and tumor prior location with 2D-Unet architecture to explore
22 the performance of training and testing using multiple 2D and 3D MRI sequences including 2D T₁-
23 weighted, 2D T₂-weighted and 3D balanced SSFP imaging protocols ¹³⁴.
24
25
26
27
28
29
30
31

32 Automated segmentation of UM in MRI has been virtually neglected thus far. Preliminary
33 data were reported using a fully automatic framework to obtain tumor thickness from 7.0 T MRI
34 images, with four cases being evaluated qualitatively ¹³⁵. A weakly-supervised deep learning
35 framework was recently published that explored the use of 2D and 3D-Unet architectures in T₁- and
36 T₂-weighted sequences in 24 patients with UM ¹³⁶. This approach demonstrated the ability of weak
37 labels (presence or absence of tumor) to generate further training data for segmentation purposes.
38
39
40
41
42
43

44 ***Unmet needs of ocular tumour segmentation*** 45

46 The automatic extraction of quantitative and reliable information on patient-specific eye
47 structures and ocular tumors (location, size, texture, morphology and distribution of pathological
48 tissues) would be a breakthrough for current diagnosis, follow-up and therapy planning. Robust and
49 accurate MReye analysis methods would help integrate multiple ophthalmic image modalities
50 covering different scales in space (such as MRI, funduscopy, OCT and ultrasound) in support of
51 patient care. Specifically, a precise characterization of ocular tumor features would boost
52 developments in the emerging field of radiogenomics ^{137,138} where the link between genetic
53 information of tumor tissue and image-based features could provide new insights into patient
54 response to therapy, and further support patient-specific treatment. Furthermore, accurate 3D eye
55
56
57
58
59
60

1
2
3 and ocular tumor segmentation would directly benefit current targeting procedures such as
4 radiation therapies applied in UM in adults.^{12,139,140} In this context, the 3D segmentation of the gross
5 tumor volume would certainly increase the acceptance of MRI for therapy planning¹³⁹ and could
6 subsequently drive a shift away from the current standard of invasive surgery, towards non-invasive
7 procedures.
8
9

10
11 Overall, current image processing methods tailored for automated eye MR image analysis
12 are limited. The methods developed thus far are not yet ready to be seamlessly integrated into
13 routine clinical practice as ready-to-use solutions. A major bottleneck in MReye analysis research is
14 the lack of available datasets with ground truth annotations, contrary to other research areas such
15 as brain tumours or multiple sclerosis, where tremendous efforts have been made to collect and
16 share data publicly to further machine learning approaches^{141,142}. Nevertheless, the increasing
17 adoption of MReye in research and clinical studies, together with the expanding embrace of novel
18 machine learning techniques promises to close this gap.
19
20
21
22
23
24
25
26

27 **Pushing the boundaries of MReye technology**

30 ***(Ultra)high field MReye***

31
32 MReye has progressed rapidly, with new research directions often being driven by the
33 sensitivity gain afforded by high field ($B_0 \geq 3.0$ T) and ultrahigh field (UHF) MRI ($B_0 \geq 7.0$ T)
34 ^{5,24,34,43,45,55,103,108,112,143-152}. An in-plane spatial resolution of 100 μm , and a voxel resolution of 200 μm
35 x 200 μm x 400 μm were achieved in vivo for gradient echo imaging at 7.0 T within clinically
36 acceptable scan times^{5,34}. Ex vivo examinations of the human eye at 9.4 T achieved an in-plane
37 spatial resolution of 32-50 μm ^{34,112}.
38
39
40
41

42 Arguably, the potential of ultrahigh field MReye remains untapped. However, this potential
43 can be restricted by a number of concomitant physics-related phenomena and practical obstacles
44 associated with magnetic field inhomogeneities at higher field strengths. These include off-
45 resonance artifacts, dielectric effects and RF non-uniformities, as well as localized tissue heating and
46 RF power deposition constraints. These effects pose serious challenges to compete with the
47 capabilities of MReye at 1.5 T. If these practical impediments can be overcome, UHF-MReye
48 promises to become a springboard for bridging critical gaps in space in time: from the near
49 molecular level to the anatomic structures of the ocular system, and from microseconds in tracking
50 Brownian motion of water, to potentially years in population imaging studies. This opens a window
51 into the eye, and into (patho)physiological processes that have, to date, been largely inaccessible.
52
53
54
55
56
57
58
59
60

Development of novel MR detector technology

MRI of subtle ocular structures requires sub-millimeter spatial resolution over a small field of view (FOV). Figure 8 shows a clinical set-up comprising a volume head RF coil in conjunction with a small surface receive RF coil. Using this approach has even more impact on improving SNR than increasing the magnetic field strength. The correct positioning of the surface RF coil is crucial¹⁵³. This requires highly experienced medical staff in the MR operator room, since the RF coil must be positioned in direct contact with the patient's face and may not be well tolerated. Despite this, the use of a small surface RF coil and a volume head RF coil together in one examination can be beneficial to obtain high-resolution anatomical images and functional images in a single session.

The SNR gains inherent to UHF MRI can be translated into enhanced spatial resolution. To meet this goal various RF antenna configurations used for MR signal excitation or/and signal reception have been proposed^{143,154,155}. Pioneering developments include a six-element transceiver RF coil array (Figure 9) that covers both eyes^{5,39,55}. This design meets the RF power deposition limit requirements of MRI, is duly certified and approved for clinical use by a notified body and provides image quality suitable for in vivo use together with optimized patient comfort and ease of use (Figure 9). To foster swift translation of this enabling RF coil technology into the clinical realm, patients with ocular masses and/or retinal detachment were examined in clinical feasibility studies (Figure 9). These investigations demonstrated enhanced spatial resolution at 7.0 T compared to clinical counterparts at 1.5 T and 3.0 T. For example, a voxel size of approximately 0.1 mm³ was achieved for diffusion weighted imaging (DWI) of the eye using a single average acquisition. This corresponds to a factor of forty improvement in spatial resolution compared to clinical protocols used at 1.5 T, and approaches the resolution of ex vivo MR microscopy at 9.4 T, which permits a voxel size of 0.003 mm³ for DWI³⁴. For comparison, in vivo DWI-MREye at 1.5 T reported using 8-10 averages to support a spatial resolution with a voxel size of 4 mm³, while a 3.0 T setup afforded a voxel size of 1.2 mm³ in a single average DWI acquisition¹⁵³. Owing to the water diffusion sensitivity inherent to DWI together with the spatial resolution enhancement, MREye at 7.0 T showed clear benefits for the differentiation between ocular tumors and retinal detachment³⁴.

Progress in gradient coil technology

MRI of subtle ocular structures requires sub-millimeter spatial resolution over a small FOV, which is constrained by the magnetic field gradients. Magnetic field gradient strength limitations on clinical scanners require long echo times (TE) for DWI of the eye and orbit to accommodate the increased diffusion encoding times needed for higher b-values, exponentially lowering the SNR of the acquisition. The advent of high performance gradient coil systems (G_{\max} =300 mT/m) for clinical

1
2
3 MR instruments enables smaller FOVs, substantially reduces TE and boosts SNR, compared to
4 conventional gradient systems, as demonstrated for ultrahigh b-value DWI of the brain^{156,157}. This
5 progress in gradient coil technology has triggered the implementation of high performance clinical
6 gradients offering $G_{\max_combined}=100$ mT/m¹⁵⁸ or $G_{\max}=113$ mT/m¹⁵⁹. This technology has multiple
7 benefits for high resolution imaging, rapid imaging and DWI of the eye and orbit.
8
9
10
11
12

13 ***Advancing rapid MR imaging techniques***

14
15 The quality of high spatial resolution ocular imaging can be hampered by involuntary eye
16 motion, and especially eye blinking. Scanning while the subject's eyes are closed is not a solution,
17 since unintentional eye movement may corrupt the imaging data. Possible solutions to reduce bulk
18 motion induced imaging artifacts include automated eye blink detection, external eye motion
19 tracking guidance or the use of rapid or accelerated imaging techniques^{34,55,148}. Echo planar imaging
20 (EPI) techniques are the most widely applied rapid MRI techniques. Notwithstanding its ubiquity, EPI
21 is prone to magnetic susceptibility artefacts that result in signal voids and image distortion. These
22 effects increase with magnetic field strength, and are especially pronounced in cranial regions
23 proximal to air filled cavities, including the paranasal sinuses and maxillary sinuses, and in close
24 proximity to skin/muscle/bone/brain boundaries including the orbit, which is particularly susceptible
25 to geometric distortions. This constitutes a severe challenge for EPI of the eye and orbit^{153,160}. RARE
26 techniques provide an alternative for rapid MR eye with high anatomic fidelity¹⁶¹⁻¹⁶³. RARE uses a
27 train of refocusing RF pulses, resulting in a handicap of imaging speed and RF power deposition
28 compared to EPI. To address these constraints, Combined Acquisition Techniques (CAT) employ a
29 RARE-EPI hybrid that integrates the anatomical integrity of RARE with the imaging speed and RF
30 power deposition advantages of EPI¹⁶⁴. RARE-EPI maintains the immunity to B_0 inhomogeneities
31 reported for RARE imaging and has the capability to acquire high fidelity, distortion-free images of
32 the eye and the orbit. This is beneficial for the assessment of ocular masses and pathologic changes
33 of the eye and the orbit⁵⁵. Owing to the reduced RF power deposition, RARE-EPI was demonstrated
34 to enhance the spatial coverage and to promote imaging speed for MR eye using simultaneous multi-
35 slice (multiband) imaging techniques⁵⁵.
36
37
38
39
40
41
42
43
44
45
46
47
48
49

50 Dynamic techniques are an intriguing alternative for rapid MR eye. The feasibility of near-
51 real-time oculodynamic MRI was demonstrated for depicting the extraocular muscles. Eye
52 movements were tracked in the horizontal and sagittal plane with a temporal resolution of 180 ms
53 per image. Analysis of real-time MRI data obtained from patients with diplopia correlated with
54 clinical testing, and may render real time MRI of the eye suitable to examine bulb motility and
55 extraocular muscle structural or functional deteriorations¹⁶⁵. A frame rate of 18 images per second
56
57
58
59
60

1
2
3 was achieved for dynamic imaging of the eye, optic nerve, and extraocular muscles using golden
4 angle radial MRI¹⁶⁶. This approach facilitated analysis of the motion enabled estimation of
5 trajectories, lengths, and strains on the optic nerves and extraocular muscles¹⁶⁶.
6
7
8
9

10 **MR safety**

11 Pushing to higher magnetic field strengths with UHF-MReye presents the same safety
12 challenges as the advent of UHF imaging technology for other systems, and must be thoroughly
13 tested for potential physiological impact and physical effects. Deepening our understanding of the
14 interactions between passively conducting implants and RF fields will be key to clinical applications.
15 An increasing number of patients have implants that might limit their access to UHF-MR, until it has
16 been conclusively demonstrated that these are safe at $B_0 \geq 7.0$ T. Many such implants have already
17 been deemed MR-safe at lower magnetic fields, but still require collecting extra data at UHF-MR.
18 Assessment of MR safety and MR compatibility at $B_0 \geq 7.0$ T has been carried out on tantalum
19 markers used in proton beam therapy (PRT) for intraocular tumors¹⁵ and for intra-ocular lenses used
20 for the treatment of cataract¹⁶⁷. These studies revealed that all ocular tantalum markers
21 commercially available today with CE certification for PT can be considered safe for MR at field
22 strengths of up to and including 7.0 T¹⁵. It was also concluded that all the tested intraocular lenses
23 currently in clinical use are considered safe for MRI up to and including 7.0 T.¹⁶⁷ Meanwhile, a large
24 body of literature exists on the MR safety of passive conductive implants at 7.0 T.¹⁶⁸⁻¹⁷⁶
25
26
27
28
29
30
31
32
33
34
35
36

37 **Looking Beyond the Horizon**

38 **Google Maps for Ocular Health**

39 Breaking new spatial and temporal boundaries and lowering detection levels with UHF-
40 MReye are some of the elements inspiring the concept of '*Google Maps for Ocular Health*'¹⁷⁷.
41 Considering how Google Maps works, one can start with a very high level view of a city, zoom in to
42 smaller neighborhoods and even view it at the scale of individual houses. However, this static spatial
43 view is not sufficient to predict what will happen in the future because other kinds of dynamic
44 information are needed. Keeping with the city example, if one wants to predict how the weather will
45 change, a static map is not sufficient. Other kinds of quantitative information, for example maps of
46 wind speed and barometric pressure, need to be integrated with the spatial views, to make a
47 weather forecast or storm alert. Analogously, predicting ocular health outcomes requires zooming in
48 to view the ophthalmic system at multiple spatial scales, and going beyond MR imaging to the level
49 of molecules, where events that are crucial to health take place. However this cannot be easily done
50
51
52
53
54
55
56
57
58
59
60

1
2
3 because different scales of images and imaging modalities (from the macro- and mesoscopic MR to
4 the micro- and sub-microscopic) need to be integrated and connected using the tools of data science
5 ^{146,178}. This requires combining different types of information, for example about water diffusion and
6 ion concentration in the eye, in order to integrate multi-scale imaging into a coherent picture to
7 develop new approaches for diagnosis and for early interception of ocular disease.
8
9
10
11
12

13 ***Electrolyte Mapping***

14
15 Each new MReye approach adds another dimension to our view of the eye that helps
16 integrate our knowledge of events at the molecular scale with effects at higher levels. The sensitivity
17 gain of UHF-MReye helps to move beyond conventional ¹H-MRI to study other MR nuclei that are
18 relevant to physiology and metabolism. For example, sodium (Na⁺) ions are an important
19 component of the VH, and play a key role in various physiological processes in the eye. The VH
20 functions as a metabolic buffer and a diffusion barrier between the anterior and the posterior
21 segments of the eye, adjoining the retina and ciliary body. The concentration of Na⁺ in the VH is
22 close to that of plasma (~150 mmol/l). Changes in concentration of substances in the vitreous body
23 likely reflect pathological processes in adjoining tissues. A recent study demonstrated the feasibility
24 of millimeter-scale spatial resolution Na⁺ imaging *in vivo* at 7.0 tesla using a dedicated six-channel
25 transceiver array tuned to the resonant frequency of ²³Na ¹⁵⁰. Three most important eye
26 compartments in the context of Na⁺ physiology were clearly delineated in the sodium images: the
27 VH, the aqueous humor and the lens (Figure 9). These results provide encouragement for ²³Na-MRI
28 research into eye diseases including ocular melanoma, cataract and glaucoma. Other x-nuclei
29 ophthalmic MRI applications emerging from basic research include fluorine (¹⁹F) MRI for probing
30 inflammation, for tracking orbital immune cell infiltration and for monitoring the bioavailability of
31 fluorinated drugs ^{179,180}. Potassium (³⁹K) MRI is also conceptually appealing for eye research since it
32 facilitates probing the potassium ion homeostasis *in vivo* ^{181,182}.
33
34
35
36
37
38
39
40
41
42
43
44
45
46

47 ***Looking towards the future of ultrahigh field MReye***

48 Each increase in magnetic field strength pushes the boundaries of MReye, and will help to
49 translate the discoveries from basic research into the clinic. Pioneering reports on brain MRI at 10.5
50 T provide a powerful stimulus for MReye at extreme magnetic field strengths ^{183,184}. The UHF-MR
51 community has already taken further steps into the future by demonstrating the feasibility of human
52 MR at 14.0 T and at 23.5 T (f=1 GHz) using numerical simulations ^{185,186}. For example, the sensitivity
53 gain at 20.0 T is expected to reduce scan times for sodium MReye by a factor of 8 versus current 7.0
54 T capabilities, and promises ²³Na imaging with an isotropic sub-millimeter spatial resolution in 5 min
55
56
57
58
59
60

1
2
3 scan time ^{187,188}. Newer horizontal preclinical MR systems operating at 15.2 - 17.2 T indicate the
4 imminent need to move towards extreme field MR (eMR). Recent reports have also emphasized the
5 value of preclinical MR at 17.6 T ¹⁸⁹⁻¹⁹⁵ and at 21.1 T ^{181,196-205}.
6
7
8
9

10 **Conclusion**

11
12 Ophthalmic imaging takes advantage of a broad spectrum of modalities, each offering a
13 multitude of benefits: tissue contrast, resolution, wave length, investigation time, invasiveness,
14 surgical compatibility, cost, etc. MReye has proven its usefulness in preclinical and clinical research
15 applications, and will come to have a role in routine clinical practice, complementing existing
16 diagnostic and prognostic tools, and even going beyond their limitations. MReye has opened an
17 unprecedented window into novel aspects of the ocular system that will help to reveal new
18 dimensions of physiology and disease.
19
20
21
22
23
24
25
26
27
28
29
30
31
32
33
34
35
36
37
38
39
40
41
42
43
44
45
46
47
48
49
50
51
52
53
54
55
56
57
58
59
60

Acknowledgements

Thoralf Niendorf wishes to thank the team at the Berlin Ultrahigh Field Facility (B.U.F.F.) at the Max-Delbrück Center for Molecular Medicine in the Helmholtz Association, Berlin, Germany for providing examples of their pioneering work, for technical assistance, support and numerous fruitful discussions. Jan-Willem Beenakker thanks the researchers at the C.J. Gorter Center for High Field MRI (Leiden, The Netherlands) for their contributions, and the radiologists and ophthalmologists of the Leiden University Medical Center (Leiden, The Netherlands) for their enthusiasm and support to explore new clinical applications of MReye. Oliver Stachs acknowledges the contributions of the team at the Core Facility Multimodal Small Animal Imaging of the University Medical Center and at the Department Life, Light & Matter at the University Rostock (Rostock, Germany). Meritxell Bach Cuadra wishes to thank A. Pica, P. Maeder, C. Ciller, H. Nguyen, R. Snitzmann, H. Kebiri, the Swiss Cancer Research foundation and the Hasler foundation.

Declaration of Interest Statement

Thoralf Niendorf is founder and CEO of MRI.TOOLS GmbH, Berlin, Germany.

Jan-Willem M. Beenakker reports research support from Philips Healthcare, Best, The Netherlands.

Table 1.

Survey of the pathologies encountered in the eye and orbital cavity warranting high-resolution MR imaging.

Ocular pathologies	Orbital pathologies
<i>Hemangioma</i>	<i>Capillary and cavernous hemangioma</i>
<i>Leiomyoma</i>	<i>Optic pathway glioma</i>
<i>PHPV, persistent hyperplastic primary vitreous</i>	<i>Optic nerve sheath meningioma</i>
<i>Uveal melanoma</i>	<i>Optic nerve neuritis</i>
<i>Choroidal metastasis</i>	<i>Benign mixed tumor</i>
<i>Coloboma/Staphyloma</i>	<i>Dacryoadenitis</i>
	<i>Dacryocystitis</i>
	<i>Eye lid tumours</i>
	<i>Cellulitis</i>
	<i>Subperiosteal abscess</i>
	<i>Mucocele & Pyocele</i>
	<i>Myasthenia Gravis</i>
	<i>Dermoid cyst</i>
	<i>Lymphoma</i>
	<i>Lymphangioma</i>
	<i>Schwannoma</i>
	<i>Orbital metastasis</i>
	<i>Idiopathic inflammatory orbital disease (Pseudotumor orbitae)</i>
	<i>Thyroid associated orbitopathy</i>

Figure Captions

Figure 1:

- A) MRI of ocular tumors. Left: Two-dimensional T_1 -weighted and T_2 -weighted imaging of retinoblastoma using a magnetic field strength of 3.0 tesla and radiofrequency head coil for signal reception (courtesy of Prof. P. Maeder, Lausanne University Hospital, Switzerland). Right: T_1 -weighted and T_2 -weighted imaging of uveal melanoma using a magnetic field strength of 1.5 tesla and a surface radiofrequency coil for signal reception (courtesy of Dr. A. Pica, Paul Scherrer Institute, Switzerland).
- B) Three-dimensional MR eye and ophthalmic imaging of a Uveal Melanoma patient. Top row: T_2 (left), T_1 (middle) and Gadolinium contrast enhanced T_1 (right) weighted images, showing the tumor (*), retinal detachment (white arrow) and sclera (black arrow) with high contrast. Bottom row: Examples of Ultrasound (left), fundus photography (middle) and whole eye coverage 3D MR eye (right) used for tumor visualisation.

Figure 2:

Three dimensional patient-specific MR eye models for proton beam therapy and for refractive surgery planning. A) 3D 7.0 tesla MR eye model (left) from a patient with Uveal Melanoma which is used for Proton Therapy dose planning (right). (courtesy of E. Fleury, Erasmus Medical Center, Rotterdam and HollandPTC, The Netherlands). B) MR-based eye-model used for optical ray-tracing simulations in which MR eye is used to personalize the retinal shape (purple), pupil plane (green) and intra-ocular lens location (red).

Figure 3:

Quantitative MR eye: A) Apparent diffusion coefficient (ADC) map of a healthy subject obtained from a series of diffusion weighted (DWI) images. B) Water content (left) and fat-quantification (right) of a Graves' Orbitopathy patient, showing not only the enlarged extra-ocular muscles (white arrow, left), but also an increased fat-fraction in the right lateral muscle (black arrow, right). C) Perfusion Weighted Imaging (PWI) using T_1 -weighted contrast enhancement, showing a contrast agent wash-out curve for a uveal melanoma patient.

Figure 4:

- A) Two patients with a mass lesion behind the globe. The standard T_1 -weighted images revealed similar signal characteristics of the mass whereas slightly different signal characteristics in the T_2 -weighted images were observed. Both lesions show increased signal after contrast injection. Although the DWI image of the top row patient is distorted, it indicates no or little restricted diffusion. The DWI image of the patient at the bottom row indicates marked restricted diffusion,

confirmed by ADC-measurements, which suggests a malignant pathology. Follow-up and histopathology revealed a cavernous hemangioma for top row the patient and an orbital metastasis due to breast cancer for the bottom row patient below.

- B) T₂-weighted images (top), DWI (center) and ADC-map (bottom) of a patient with giant cell arteritis and acute onset of vision loss. Distortion-free DWI depicted restricted diffusion in the right optic nerve (center, arrow), indicating ischemia.

Figure 5

Contrast distribution in a pig eye *ex vivo* after administration of gadolinium-based contrast agent. All images were acquired at 7.0 tesla (T₁-weighted spin-echo sequence, TR=550 ms, TE=14 ms, slice thickness=0.7 mm, FOV=40 x 40 mm², matrix size=1024 x 1024, acquisition time 8:42min) after administration of gadolinium-based contrast agent (0.5 mmol/l; 1:128 with 0.9% saline). a) after subcorneal injection of 50 µl contrast agent, b) immediately after installation of 2ml of contrast agent in the anterior chamber, c) the same as in b) but 45 min after contrast application; the eye was imaged placed on the cornea leading to deformity and d) after continuous flushing of the anterior chamber with contrast agent for 30 min and artificial drainage in the posterior chamber.

Figure 6

Examples of MR microscopy.

- A) Left: Axial T₂-weighted image of a human eye *ex vivo* at 7.0 T; MR microscopy allows the depiction of the three layers of the globe: sclera – arrow, choroid – dotted arrow, retina – arrowhead; x – lens. Right: Axial T₂-weighted image of a human optic nerve *ex vivo* at 9.4T; MR microscopy at this field strength depicts the layers of the optic nerve and the central artery (x); sclera – arrow, choroid – dotted arrow, retina – arrowhead. The corresponding diffusion tensor image (DTI) of the human optic nerve *ex vivo* at 9.4T is shown below using colour coding (green: anterior-posterior; blue: cranial-caudal; red: right-left).
- B) MR microscopy of uveal melanoma *ex vivo*. Left: Sagittal T₂-weighted image demonstrating the posterior extend of the tumor (x) with subsequent retinal (arrow) and choroidal (dotted arrow) detachment. The tumor infiltrates the ciliary body (arrowhead). Right) Coronal T₂-weighted image demonstrating the extension of the tumor (x) from 10 – 2 o'clock with infiltration of the iris (arrow). Low intensities (dotted arrow) representing the melanin-producing tumor parts
- C) In vivo MR microscopy of the optic nerve at 7.0 T using a dedicated 6-channel radio-frequency coil array for signal detection. Left: Coronal T₁-weighted 3D image of a healthy subject. Right: corresponding conventional histology (HE-stain, 10x magnification) of a patient. long arrow: inferior rectus muscle; dotted arrow: medial rectus muscle; arrowhead: superior rectus muscle; short arrow: levator palpebrae muscle; green arrow: superior oblique muscle; red arrow: lateral rectus muscle.

Figure 7 :

- A) Active Shape Model (ASM) segmentation pipeline: healthy eye (top row) and eye with retinoblastoma (RB, bottom row). Pre-processing is needed to determine a volume of interest; ASM mean average shape superimposed to the eye to be segmented; illustration of the different modes of variation: mean shape (\bar{x}) of the sclera (upper left) and the vitreous humor and the lens (down left) and b1, b2, b3, and b4 are the 1st, 2nd, 3th and 4th mode of variation respectively (effects in shape deformation colored in mm with respect to the distance to the mean shape); automatic fitting is done based on MR image information. Resulting segmentation for the lens, sclera and vitreous humour. Figure adapted from ¹²⁶ and ²⁰⁶.
- B) Left: 3D patient specific eye model of a patient with UM, based on manual delineation. Right: Results of automated UM segmentation. 1st and 2nd row show a T₁-weighted and a T₂-weighted MR respectively, automated segmentation is highlighted in solid green, manual segmentation is outlined in red. Blue arrows show that automatic segmentation can better fit image contours than manual segmentation; yellow arrows show areas where automated segmentation cannot separate tumor and retinal detachment. Figure adapted from ¹³⁶.

Figure 8:

- A) Photograph of a state-of-the-art radiofrequency coil set-up used in clinical practice at 1.5 T and 3.0 T. The small surface RF receive coil is used to obtain high-resolution images of the eye and orbit. The head RF coil is used to acquire functional images such as DWI and PWI.
- B) Left: Photographs of an early version of a six channel TX/RX array tailored for ocular imaging at 7.0 T (f=297 MHz) showing the coil casing and a mirror which allows for fixating a point in the isocenter of the scanner bore. Right: Photographs of an advanced version of a six channel TX/RX array tailored for ocular imaging at 7.0 T (f=297 MHz) showing the (i) coil casing, (ii) an universal interface to ensure patient comfort and ease of use and to connect the RF coil array with the scanner and (iii) a mirror which allows for fixating a point in the isocenter of the scanner bore. (Courtesy of Dr. Helmar Waiczies and Dr. Andre Kühne, MRI.TOOLS GmbH, Berlin, Germany.)
- C) Left: Examples of MRI of the eye of a healthy subject obtained at a magnetic field strength of 7.0 T using a six-channel RF array for signal transmission and reception. Top: T₁-weighted 3D gradient-echo imaging (spatial resolution (0.3 x 0.3x1.0) mm³, scan time 3:12 min, echo time TE=3.6 ms, repetition time TR=10.3 ms, flip angle $\alpha=6^\circ$, matrix size = (320 x 230), FOV=(81 x 58) mm². Bottom: T₂-weighted imaging using a RARE (fast spin-echo) technique (spatial resolution (0.25 x 0.25 x 0.7) mm³, TR=2940 ms, TE=85 ms, refocusing pulse $\alpha=100^\circ$, FOV = (84 x 60) mm², matrix size = 384 x 245, number of slices = 6, number of averages = 4, scan time = 2:00 min per average. Right: Examples of MRI of the eye of a subject with uveal melanoma. Images were obtained after Cyberknife intervention at a magnetic field strength of 7.0 T using a six-channel RF array for signal transmission and reception. Top: T₁-weighted 3D gradient-echo imaging,

1
2
3
4 Bottom: T₂-weighted fast spin-echo imaging (RARE). The membrane between the vitreous
5 humor (hyper-intense) and the subretinal space is hypo-intense.
6
7

8 **Figure 9:**

- 9
10 A) One of the most exciting areas of MR eye concerns imaging across multiple scales in space and
11 time. Enabled by data science and artificial intelligence, one can imagine a concept like 'Google
12 Maps for ocular health', in which macroscopic, mesoscopic, and microscopic views are stitched
13 together for seamless zooming. This figure shows an example of multi-scale, multi-contrast
14 MR eye obtained for a patient with a uveal melanoma in the right eye. From left to right: *In vivo*
15 anatomical view using T₁-weighted gradient-echo MRI at 3.0 T (spatial resolution: (0.6 x 0.6 x 0.6)
16 mm³); *in vivo* anatomical view using T₂-weighted multi-shot RARE MRI at 7.0 T (spatial resolution
17 of (0.1 x 0.1 x 1.2) mm³); *in vivo* diffusion weighted imaging using a multi-shot EPI-RARE variant
18 (spatial resolution: (0.5 x 0.5 x 5) mm³); *in vivo* apparent water diffusion coefficient (ADC) map
19 derived from a series of diffusion weighted images acquired with a multi-shot EPI-RARE hybrid
20 (spatial resolution: (0.5 x 0.5 x 5) mm³) showing the retinal detachment as well as the melanoma,
21 *ex vivo* ADC map (spatial resolution of (0.1 x 0.1 x 0.3) mm³) of the enucleated eye obtained at
22 9.4 T showing strong contrast between the remaining vitreous body, the subretinal space
23 induced by retinal detachment and the ocular mass; Macrophotography of the enucleated eye.
24
25 B) Sodium (²³Na) MRI of the eye at 7.0 tesla. From left to right: ²³Na six channel transceiver RF array
26 (f=79 MHz) placed on an adult volunteer. ²³Na sagittal view (nominal isotropic resolution = (1.0 x
27 1.0 x 1.0 mm³), scan time = 14 minutes 10 seconds) of the eye of a healthy male volunteer (BMI
28 = 27.1 kg/m²) obtained with density adapted 3D projection reconstruction imaging. Colour
29 coded sodium image superimposed to the anatomical view (gray scale) derived from T₁-
30 weighted gradient-echo imaging. ²³Na axial view (nominal isotropic resolution = (1.0 x 1.0 x 1.0
31 mm³), scan time = 14 minutes 10 seconds) of the same healthy male volunteer. Colour coded
32 sodium image superimposed to the anatomical view (gray scale) obtained from T₁-weighted
33 gradient-echo imaging.
34
35
36
37
38
39
40
41
42
43
44
45
46
47
48
49
50
51
52
53
54
55
56
57
58
59
60

References:

1. Georgouli T, James T, Tanner S, et al. High-resolution microscopy coil MR-Eye. *Eye (Lond)*. Aug 2008;22(8):994-996.
2. Tsiapa I, Tsilimbaris MK, Papadaki E, et al. High resolution MR eye protocol optimization: Comparison between 3D-CISS, 3D-PSIF and 3D-VIBE sequences. *Phys Med*. Nov 2015;31(7):774-780.
3. Dobbs NW, Budak MJ, White RD, Zealley IA. MR-Eye: High-Resolution Microscopy Coil MRI for the Assessment of the Orbit and Periorbital Structures, Part 1: Technique and Anatomy. *AJNR Am J Neuroradiol*. Jun 2020;41(6):947-950.
4. Fleury E, Trnkova P, Erdal E, et al. 3D MRI-based treatment planning approach for non-invasive ocular proton therapy. *Med Phys*. Dec 17 2020.
5. Glarin RK, Nguyen BN, Cleary JO, et al. MR-EYE: High-Resolution MRI of the Human Eye and Orbit at Ultrahigh Field (7T). *Magn Reson Imaging Clin N Am*. Feb 2021;29(1):103-116.
6. Chattopadhyay C, Kim DW, Gombos DS, et al. Uveal melanoma: From diagnosis to treatment and the science in between. *Cancer*. Aug 1 2016;122(15):2299-2312.
7. Bergman L, Nilsson B, Lundell G, Lundell M, Seregard S. Ruthenium brachytherapy for uveal melanoma, 1979-2003: survival and functional outcomes in the Swedish population. *Ophthalmology*. May 2005;112(5):834-840.
8. Afshar AR, Damato BE. Uveal melanoma: evidence for efficacy of therapy. *Int Ophthalmol Clin*. Winter 2015;55(1):23-43.
9. Beenakker JW, Ferreira TA, Soemarwoto KP, et al. Clinical evaluation of ultra-high-field MRI for three-dimensional visualisation of tumour size in uveal melanoma patients, with direct relevance to treatment planning. *MAGMA*. Jun 2016;29(3):571-577.
10. Char DH, Kroll S, Stone RD, Harrie R, Kerman B. Ultrasonographic measurement of uveal melanoma thickness: interobserver variability. *Br J Ophthalmol*. Mar 1990;74(3):183-185.
11. Grech Fonk L, Ferreira TA, Webb AG, Luyten GPM, Beenakker JM. The Economic Value of MR-Imaging for Uveal Melanoma. *Clin Ophthalmol*. 2020;14:1135-1143.

- 1
2
3 **12.** Marnitz S, Cordini D, Bendl R, et al. Proton therapy of uveal melanomas: intercomparison of
4 MRI-based and conventional treatment planning. *Strahlenther Onkol.* Jul 2006;182(7):395-
5 399.
6
7
- 8 **13.** Daftari I, Aghaian E, O'Brien JM, Dillon W, Phillips TL. 3D MRI-based tumor delineation of
9 ocular melanoma and its comparison with conventional techniques. *Med Phys.* Nov
10 2005;32(11):3355-3362.
11
12
- 13 **14.** Zoberi JE, Garcia-Ramirez J, Hedrick S, et al. MRI-based treatment planning and dose delivery
14 verification for intraocular melanoma brachytherapy. *Brachytherapy.* Jan - Feb
15 2018;17(1):31-39.
16
17
- 18 **15.** Oberacker E, Paul K, Huelnhagen T, et al. Magnetic resonance safety and compatibility of
19 tantalum markers used in proton beam therapy for intraocular tumors: A 7.0 Tesla study.
20 *Magn Reson Med.* Oct 2017;78(4):1533-1546.
21
22
- 23 **16.** Jaarsma-Coes MG, Marinkovic M, Astreimidou E, et al. Measuring eye deformation between
24 planning and proton beam therapy position using magnetic resonance imaging. *Physics and*
25 *Imaging in Radiation Oncology.* 2020;16:4.
26
27
- 28 **17.** Jaeken B, Mirabet S, Marin JM, Artal P. Comparison of the optical image quality in the
29 periphery of phakic and pseudophakic eyes. *Invest Ophthalmol Vis Sci.* May 1
30 2013;54(5):3594-3599.
31
32
- 33 **18.** Smith EL, 3rd, Kee CS, Ramamirtham R, Qiao-Grider Y, Hung LF. Peripheral vision can
34 influence eye growth and refractive development in infant monkeys. *Invest Ophthalmol Vis*
35 *Sci.* Nov 2005;46(11):3965-3972.
36
37
- 38 **19.** Mutti DO, Sinnott LT, Mitchell GL, et al. Relative peripheral refractive error and the risk of
39 onset and progression of myopia in children. *Invest Ophthalmol Vis Sci.* Jan 5
40 2011;52(1):199-205.
41
42
- 43 **20.** Verkicharla PK, Mathur A, Mallen EA, Pope JM, Atchison DA. Eye shape and retinal shape,
44 and their relation to peripheral refraction. *Ophthalmic Physiol Opt.* May 2012;32(3):184-199.
45
46
- 47 **21.** Lim LS, Matsumura S, Htoon HM, et al. MRI of posterior eye shape and its associations with
48 myopia and ethnicity. *Br J Ophthalmol.* Dec 2 2019.
49
50
- 51 **22.** Atchison DA, Pritchard N, Schmid KL, Scott DH, Jones CE, Pope JM. Shape of the retinal
52 surface in emmetropia and myopia. *Invest Ophthalmol Vis Sci.* Aug 2005;46(8):2698-2707.
53
54
55
56
57
58
59
60

- 1
 - 2
 - 3
 - 4
 - 5
 - 6
 - 7
 - 8
 - 9
 - 10
 - 11
 - 12
 - 13
 - 14
 - 15
 - 16
 - 17
 - 18
 - 19
 - 20
 - 21
 - 22
 - 23
 - 24
 - 25
 - 26
 - 27
 - 28
 - 29
 - 30
 - 31
 - 32
 - 33
 - 34
 - 35
 - 36
 - 37
 - 38
 - 39
 - 40
 - 41
 - 42
 - 43
 - 44
 - 45
 - 46
 - 47
 - 48
 - 49
 - 50
 - 51
 - 52
 - 53
 - 54
 - 55
 - 56
 - 57
 - 58
 - 59
 - 60
23. Pope JM, Verkicharla PK, Sepehrband F, Suheimat M, Schmid KL, Atchison DA. Three-dimensional MRI study of the relationship between eye dimensions, retinal shape and myopia. *Biomed Opt Express*. May 1 2017;8(5):2386-2395.
24. Richdale K, Bullimore MA, Sinnott LT, Zadnik K. The Effect of Age, Accommodation, and Refractive Error on the Adult Human Eye. *Optom Vis Sci*. Jan 2016;93(1):3-11.
25. Beenakker JW, Shamonin DP, Webb AG, Luyten GP, Stoel BC. Automated retinal topographic maps measured with magnetic resonance imaging. *Invest Ophthalmol Vis Sci*. Jan 15 2015;56(2):1033-1039.
26. van Vught L, Dekker CE, Stoel BC, Luyten GPM, Beenakker JWM. Evaluation of intraocular lens position and retinal shape in negative dysphotopsia using high-resolution MRI. *ACTA OPHTHALMOLOGICA*. 2020;98:1.
27. Ferreira TA, Saraiva P, Genders SW, Buchem MV, Luyten GPM, Beenakker JW. CT and MR imaging of orbital inflammation. *Neuroradiology*. Dec 2018;60(12):1253-1266.
28. Gokharman D, Aydin S. Magnetic Resonance Imaging in Orbital Pathologies: A Pictorial Review. *J Belg Soc Radiol*. Jan 4 2018;101(1):5.
29. Strijkers GJ, Araujo ECA, Azzabou N, et al. Exploration of New Contrasts, Targets, and MR Imaging and Spectroscopy Techniques for Neuromuscular Disease - A Workshop Report of Working Group 3 of the Biomedicine and Molecular Biosciences COST Action BM1304 MYO-MRI. *J Neuromuscul Dis*. 2019;6(1):1-30.
30. Weber MA, Zoubaa S, Schlieter M, et al. Diagnostic performance of spectroscopic and perfusion MRI for distinction of brain tumors. *Neurology*. Jun 27 2006;66(12):1899-1906.
31. Sepahdari AR, Politi LS, Aakalu VK, Kim HJ, Razek AA. Diffusion-weighted imaging of orbital masses: multi-institutional data support a 2-ADC threshold model to categorize lesions as benign, malignant, or indeterminate. *AJNR Am J Neuroradiol*. Jan 2014;35(1):170-175.
32. Ren J, Yuan Y, Wu Y, Tao X. Differentiation of orbital lymphoma and idiopathic orbital inflammatory pseudotumor: combined diagnostic value of conventional MRI and histogram analysis of ADC maps. *BMC Med Imaging*. May 2 2018;18(1):6.
33. Elkhamary SM, Galindo-Ferreiro A, AlGhafri L, Khandekar R, Schellini SA. Characterization of diffuse orbital mass using Apparent diffusion coefficient in 3-tesla MRI. *Eur J Radiol Open*. 2018;5:52-57.

- 1
2
3
4
5
6
7
8
9
10
11
12
13
14
15
16
17
18
19
20
21
22
23
24
25
26
27
28
29
30
31
32
33
34
35
36
37
38
39
40
41
42
43
44
45
46
47
48
49
50
51
52
53
54
55
56
57
58
59
60
34. Paul K, Graessl A, Rieger J, et al. Diffusion-sensitized ophthalmic magnetic resonance imaging free of geometric distortion at 3.0 and 7.0 T: a feasibility study in healthy subjects and patients with intraocular masses. *Invest Radiol*. May 2015;50(5):309-321.
 35. Das T, Roos JCP, Patterson AJ, Graves MJ, Murthy R. T2-relaxation mapping and fat fraction assessment to objectively quantify clinical activity in thyroid eye disease: an initial feasibility study. *Eye (Lond)*. Feb 2019;33(2):235-243.
 36. Keene KR, van Vught L, van de Velde NM, et al. The feasibility of quantitative MRI of extraocular muscles in myasthenia gravis and Graves' orbitopathy. *NMR Biomed*. Sep 7 2020:e4407.
 37. Mafee MF, Rapoport M, Karimi A, Ansari SA, Shah J. Orbital and ocular imaging using 3- and 1.5-T MR imaging systems. *Neuroimaging Clin N Am*. Feb 2005;15(1):1-21.
 38. Lemke AJ, Alai-Omid M, Hengst SA, Kazi I, Felix R. Eye imaging with a 3.0-T MRI using a surface coil--a study on volunteers and initial patients with uveal melanoma. *Eur Radiol*. May 2006;16(5):1084-1089.
 39. Graessl A, Muhle M, Schwerter M, et al. Ophthalmic magnetic resonance imaging at 7 T using a 6-channel transceiver radiofrequency coil array in healthy subjects and patients with intraocular masses. *Invest Radiol*. May 2014;49(5):260-270.
 40. Lindner T, Langner S, Graessl A, et al. High spatial resolution in vivo magnetic resonance imaging of the human eye, orbit, nervus opticus and optic nerve sheath at 7.0 Tesla. *Exp Eye Res*. Aug 2014;125:89-94.
 41. Posch H, Erb-Eigner K. [Magnetic Resonance Imaging of the Orbital Cavity: Indications and Diagnostic Possibilities]. *Klin Monbl Augenheilkd*. Mar 2019;236(3):321-339.
 42. Ferreira TA, Pinheiro CF, Saraiva P, et al. MR and CT Imaging of the Normal Eyelid and its Application in Eyelid Tumors. *Cancers (Basel)*. Mar 12 2020;12(3).
 43. Jaarsma-Coes MG, Goncalves Ferreira TA, van Haren GR, Marinkovic M, Beenakker JM. MRI enables accurate diagnosis and follow-up in uveal melanoma patients after vitrectomy. *Melanoma Res*. Dec 2019;29(6):655-659.
 44. Politi LS, Godi C, Cammarata G, et al. Magnetic resonance imaging with diffusion-weighted imaging in the evaluation of thyroid-associated orbitopathy: getting below the tip of the iceberg. *Eur Radiol*. May 2014;24(5):1118-1126.

- 1
 - 2
 - 3
 - 4
 - 5
 - 6
 - 7
 - 8
 - 9
 - 10
 - 11
 - 12
 - 13
 - 14
 - 15
 - 16
 - 17
 - 18
 - 19
 - 20
 - 21
 - 22
 - 23
 - 24
 - 25
 - 26
 - 27
 - 28
 - 29
 - 30
 - 31
 - 32
 - 33
 - 34
 - 35
 - 36
 - 37
 - 38
 - 39
 - 40
 - 41
 - 42
 - 43
 - 44
 - 45
 - 46
 - 47
 - 48
 - 49
 - 50
 - 51
 - 52
 - 53
 - 54
 - 55
 - 56
 - 57
 - 58
 - 59
 - 60
45. Ro SR, Asbach P, Siebert E, Bertelmann E, Hamm B, Erb-Eigner K. Characterization of orbital masses by multiparametric MRI. *Eur J Radiol.* Feb 2016;85(2):324-336.
46. Kapur R, Sepahdari AR, Mafee MF, et al. MR imaging of orbital inflammatory syndrome, orbital cellulitis, and orbital lymphoid lesions: the role of diffusion-weighted imaging. *AJNR Am J Neuroradiol.* Jan 2009;30(1):64-70.
47. Fatima Z, Ichikawa T, Ishigame K, et al. Orbital masses: the usefulness of diffusion-weighted imaging in lesion categorization. *Clin Neuroradiol.* Jun 2014;24(2):129-134.
48. Politi LS, Forghani R, Godi C, et al. Ocular adnexal lymphoma: diffusion-weighted mr imaging for differential diagnosis and therapeutic monitoring. *Radiology.* Aug 2010;256(2):565-574.
49. Sepahdari AR, Aakalu VK, Setabutr P, Shiehmorteza M, Naheedy JH, Mafee MF. Indeterminate orbital masses: restricted diffusion at MR imaging with echo-planar diffusion-weighted imaging predicts malignancy. *Radiology.* Aug 2010;256(2):554-564.
50. Lope LA, Hutcheson KA, Khademian ZP. Magnetic resonance imaging in the analysis of pediatric orbital tumors: utility of diffusion-weighted imaging. *J AAPOS.* Jun 2010;14(3):257-262.
51. Sepahdari AR, Aakalu VK, Kapur R, et al. MRI of orbital cellulitis and orbital abscess: the role of diffusion-weighted imaging. *AJR Am J Roentgenol.* Sep 2009;193(3):W244-250.
52. Zhang F, Sha Y, Qian J, et al. Role of magnetic resonance diffusion-weighted imaging in differentiating lacrimal masses. *J Magn Reson Imaging.* Sep 2014;40(3):641-648.
53. Foti PV, Longo A, Reibaldi M, et al. Uveal melanoma: quantitative evaluation of diffusion-weighted MR imaging in the response assessment after proton-beam therapy, long-term follow-up. *Radiol Med.* Feb 2017;122(2):131-139.
54. Ahmed Sultan A, HanyAl-backry M, Mohamed Alhefney E, Ezzat Mosa A, Elmetwally Abdallah Farahat H. Role of MR spectroscopy and diffusion-weighted imaging in diagnosis of orbital masses. *The Egyptian Journal of Radiology and Nuclear Medicine.* 2018/03/01/2018;49(1):45-53.
55. Paul K, Huelnhagen T, Oberacker E, et al. Multiband diffusion-weighted MRI of the eye and orbit free of geometric distortions using a RARE-EPI hybrid. *NMR Biomed.* Mar 2018;31(3).
56. Yuan Y, Kuai XP, Chen XS, Tao XF. Assessment of dynamic contrast-enhanced magnetic resonance imaging in the differentiation of malignant from benign orbital masses. *Eur J Radiol.* Sep 2013;82(9):1506-1511.

- 1
 - 2
 - 3
 - 4
 - 5
 - 6
 - 7
 - 8
 - 9
 - 10
 - 11
 - 12
 - 13
 - 14
 - 15
 - 16
 - 17
 - 18
 - 19
 - 20
 - 21
 - 22
 - 23
 - 24
 - 25
 - 26
 - 27
 - 28
 - 29
 - 30
 - 31
 - 32
 - 33
 - 34
 - 35
 - 36
 - 37
 - 38
 - 39
 - 40
 - 41
 - 42
 - 43
 - 44
 - 45
 - 46
 - 47
 - 48
 - 49
 - 50
 - 51
 - 52
 - 53
 - 54
 - 55
 - 56
 - 57
 - 58
 - 59
 - 60
57. Erb-Eigner K, Asbach P, Ro SR, et al. DCE-MR imaging of orbital lesions: diagnostic performance of the tumor flow residence time tau calculated by a multi-compartmental pharmacokinetic tumor model based on individual factors. *Acta Radiol.* May 2019;60(5):643-652.
58. Jiang X, Asbach P, Willerding G, et al. Dynamic contrast-enhanced MRI of ocular melanoma. *Melanoma Res.* Apr 2015;25(2):149-156.
59. Kamrava M, Sepahdari AR, Leu K, et al. Quantitative multiparametric MRI in uveal melanoma: increased tumor permeability may predict monosomy 3. *Neuroradiology.* Aug 2015;57(8):833-840.
60. Shields CL, Furuta M, Berman EL, et al. Choroidal nevus transformation into melanoma: analysis of 2514 consecutive cases. *Arch Ophthalmol.* Aug 2009;127(8):981-987.
61. Stroszczynski C, Hosten N, Bornfeld N, et al. Choroidal hemangioma: MR findings and differentiation from uveal melanoma. *AJNR Am J Neuroradiol.* Sep 1998;19(8):1441-1447.
62. Gulani V, Calamante F, Shellock FG, Kanal E, Reeder SB. Gadolinium deposition in the brain: summary of evidence and recommendations. *Lancet Neurol.* Jul 2017;16(7):564-570.
63. Boyken J, Niendorf T, Flemming B, Seeliger E. Gadolinium Deposition in the Brain after Contrast-enhanced MRI: Are the Data Valid? *Radiology.* Aug 2018;288(2):630-632.
64. Kahn J, Posch H, Steffen IG, et al. Is There Long-term Signal Intensity Increase in the Central Nervous System on T1-weighted Images after MR Imaging with the Hepatospecific Contrast Agent Gadoteric Acid? A Cross-sectional Study in 91 Patients. *Radiology.* Mar 2017;282(3):708-716.
65. Deike-Hofmann K, von Lampe P, Schlemmer HP, et al. The anterior eye chamber: entry of the natural excretion pathway of gadolinium contrast agents? *Eur Radiol.* Aug 2020;30(8):4633-4640.
66. Shatz W, Aaronson J, Yohe S, Kelley RF, Kalia YN. Strategies for modifying drug residence time and ocular bioavailability to decrease treatment frequency for back of the eye diseases. *Expert Opin Drug Deliv.* Jan 2019;16(1):43-57.
67. Shikari H, Silva PS, Sun JK. Complications of intravitreal injections in patients with diabetes. *Semin Ophthalmol.* Sep-Nov 2014;29(5-6):276-289.
68. Bishop PN. Structural macromolecules and supramolecular organisation of the vitreous gel. *Prog Retin Eye Res.* May 2000;19(3):323-344.

- 1
2
3
4
5
6
7
8
9
10
11
12
13
14
15
16
17
18
19
20
21
22
23
24
25
26
27
28
29
30
31
32
33
34
35
36
37
38
39
40
41
42
43
44
45
46
47
48
49
50
51
52
53
54
55
56
57
58
59
60
69. Del Amo EM, Rimpela AK, Heikkinen E, et al. Pharmacokinetic aspects of retinal drug delivery. *Prog Retin Eye Res.* Mar 2017;57:134-185.
 70. Das UN. Diabetic macular edema, retinopathy and age-related macular degeneration as inflammatory conditions. *Arch Med Sci.* Oct 1 2016;12(5):1142-1157.
 71. Rowe-Rendleman CL, Durazo SA, Kompella UB, et al. Drug and gene delivery to the back of the eye: from bench to bedside. *Invest Ophthalmol Vis Sci.* Apr 28 2014;55(4):2714-2730.
 72. Li SK, Lizak MJ, Jeong EK. MRI in ocular drug delivery. *NMR Biomed.* Nov 2008;21(9):941-956.
 73. Li SK, Hao J, Liu H, Lee JH. MRI study of subconjunctival and intravitreal injections. *J Pharm Sci.* Jul 2012;101(7):2353-2363.
 74. Shi X, Liu X, Wu X, Lu ZR, Li SK, Jeong EK. Ocular pharmacokinetic study using T(1) mapping and Gd-chelate- labeled polymers. *Pharm Res.* Dec 2011;28(12):3180-3188.
 75. Cheng HM, Kwong KK, Xiong J, Chang C. GdDTPA-enhanced magnetic resonance imaging of the aqueous flow in the rabbit eye. *Magn Reson Med.* Jan 1991;17(1):237-243.
 76. Ho LC, Conner IP, Do CW, et al. In vivo assessment of aqueous humor dynamics upon chronic ocular hypertension and hypotensive drug treatment using gadolinium-enhanced MRI. *Invest Ophthalmol Vis Sci.* Apr 24 2014;55(6):3747-3757.
 77. Jockovich ME, Murray TG, Clifford PD, Moshfeghi AA. Posterior juxtasclear injection of anecortave acetate: magnetic resonance and echographic imaging and localization in rabbit eyes. *Retina.* Feb 2007;27(2):247-252.
 78. Kim H, Lizak MJ, Tansey G, et al. Study of ocular transport of drugs released from an intravitreal implant using magnetic resonance imaging. *Ann Biomed Eng.* Feb 2005;33(2):150-164.
 79. Kopp F, Eickner T, Polei S, et al. Ultrahigh field MR imaging of a subconjunctival anti-glaucoma drug delivery system in a rabbit model. *Sci Rep.* Nov 17 2017;7(1):15780.
 80. Zhou H, Hernandez C, Goss M, Gawlik A, Exner AA. Biomedical Imaging in Implantable Drug Delivery Systems. *Curr Drug Targets.* 2015;16(6):672-682.
 81. Da M, Li KK, Chan KC, Wu EX, Wong DS. Distribution of Triamcinolone Acetonide after Intravitreal Injection into Silicone Oil-Filled Eye. *Biomed Res Int.* 2016;2016:5485467.
 82. Li SK, Jeong EK, Hastings MS. Magnetic resonance imaging study of current and ion delivery into the eye during transscleral and transcorneal iontophoresis. *Invest Ophthalmol Vis Sci.* Apr 2004;45(4):1224-1231.

- 1
2
3
4
5
6
7
8
9
10
11
12
13
14
15
16
17
18
19
20
21
22
23
24
25
26
27
28
29
30
31
32
33
34
35
36
37
38
39
40
41
42
43
44
45
46
47
48
49
50
51
52
53
54
55
56
57
58
59
60
- 83.** Molokhia SA, Jeong EK, Higuchi WI, Li SK. Examination of penetration routes and distribution of ionic permeants during and after transscleral iontophoresis with magnetic resonance imaging. *Int J Pharm.* Apr 20 2007;335(1-2):46-53.
- 84.** Alikacem N, Yoshizawa T, Nelson KD, Wilson CA. Quantitative MR imaging study of intravitreal sustained release of VEGF in rabbits. *Invest Ophthalmol Vis Sci.* May 2000;41(6):1561-1569.
- 85.** Berkowitz BA, Roberts R, Luan H, Peysakhov J, Mao X, Thomas KA. Dynamic contrast-enhanced MRI measurements of passive permeability through blood retinal barrier in diabetic rats. *Invest Ophthalmol Vis Sci.* Jul 2004;45(7):2391-2398.
- 86.** O'Connor JP, Jackson A, Parker GJ, Jayson GC. DCE-MRI biomarkers in the clinical evaluation of antiangiogenic and vascular disrupting agents. *Br J Cancer.* Jan 29 2007;96(2):189-195.
- 87.** Trick GL, Liggett J, Levy J, et al. Dynamic contrast enhanced MRI in patients with diabetic macular edema: initial results. *Exp Eye Res.* Jul 2005;81(1):97-102.
- 88.** Wei W, Jia G, von Tengge-Kobligk H, et al. Dynamic Contrast-Enhanced Magnetic Resonance Imaging of Ocular Melanoma as a Tool to Predict Metastatic Potential. *J Comput Assist Tomogr.* Sep/Oct 2017;41(5):823-827.
- 89.** Grade M, Hernandez Tamames JA, Pizzini FB, Achten E, Golay X, Smits M. A neuroradiologist's guide to arterial spin labeling MRI in clinical practice. *Neuroradiology.* Dec 2015;57(12):1181-1202.
- 90.** Vaghefi E, Pontre B. Application of Arterial Spin Labelling in the Assessment of Ocular Tissues. *Biomed Res Int.* 2016;2016:6240504.
- 91.** Muir ER, De La Garza B, Duong TQ. Blood flow and anatomical MRI in a mouse model of retinitis pigmentosa. *Magn Reson Med.* Jan 2013;69(1):221-228.
- 92.** Estelrich J, Sanchez-Martin MJ, Busquets MA. Nanoparticles in magnetic resonance imaging: from simple to dual contrast agents. *Int J Nanomedicine.* 2015;10:1727-1741.
- 93.** Andreou C, Pal S, Rotter L, Yang J, Kircher MF. Molecular Imaging in Nanotechnology and Theranostics. *Mol Imaging Biol.* Jun 2017;19(3):363-372.
- 94.** Raju HB, Hu Y, Padgett KR, Rodriguez JE, Goldberg JL. Investigation of nanoparticles using magnetic resonance imaging after intravitreal injection. *Clin Exp Ophthalmol.* Jan-Feb 2012;40(1):100-107.

- 1
2
3
4
5
6
7
8
9
10
11
12
13
14
15
16
17
18
19
20
21
22
23
24
25
26
27
28
29
30
31
32
33
34
35
36
37
38
39
40
41
42
43
44
45
46
47
48
49
50
51
52
53
54
55
56
57
58
59
60
95. Tzameret A, Ketter-Katz H, Edelshtain V, et al. In vivo MRI assessment of bioactive magnetic iron oxide/human serum albumin nanoparticle delivery into the posterior segment of the eye in a rat model of retinal degeneration. *J Nanobiotechnology*. Jan 10 2019;17(1):3.
96. Varshochian R, Riazi-Esfahani M, Jeddi-Tehrani M, et al. Albuminated PLGA nanoparticles containing bevacizumab intended for ocular neovascularization treatment. *J Biomed Mater Res A*. Oct 2015;103(10):3148-3156.
97. Fanea L, Fagan AJ. Review: magnetic resonance imaging techniques in ophthalmology. *Mol Vis*. 2012;18:2538-2560.
98. Chan KC, Cheung MM, Wu EX. In vivo multiparametric magnetic resonance imaging and spectroscopy of rodent visual system. *J Integr Neurosci*. Dec 2010;9(4):477-508.
99. Mangia S, Tkac I, Gruetter R, et al. Sensitivity of single-voxel ¹H-MRS in investigating the metabolism of the activated human visual cortex at 7 T. *Magn Reson Imaging*. May 2006;24(4):343-348.
100. Chow AM, Zhou IY, Fan SJ, Chan KW, Chan KC, Wu EX. Metabolic changes in visual cortex of neonatal monocular enucleated rat: a proton magnetic resonance spectroscopy study. *Int J Dev Neurosci*. Feb 2011;29(1):25-30.
101. Chan KC, So KF, Wu EX. Proton magnetic resonance spectroscopy revealed choline reduction in the visual cortex in an experimental model of chronic glaucoma. *Exp Eye Res*. Jan 2009;88(1):65-70.
102. Liu X, Li SK, Jeong EK. Ocular pharmacokinetic study of a corticosteroid by ¹⁹F MR. *Exp Eye Res*. Sep 2010;91(3):347-352.
103. Erb-Eigner K, Warmuth C, Taupitz M, Willerding G, Bertelmann E, Asbach P. Impact of magnetic field strength and receiver coil in ocular MRI: a phantom and patient study. *Rofo*. Sep 2013;185(9):830-837.
104. Atlas SW, Bilaniuk LT, Zimmerman RA, Hackney DB, Goldberg HI, Grossman RI. Orbit: initial experience with surface coil spin-echo MR imaging at 1.5 T. *Radiology*. Aug 1987;164(2):501-509.
105. Hosten N, Bornfeld N, Wassmuth R, et al. Uveal melanoma: detection of extraocular growth with MR imaging and US. *Radiology*. Jan 1997;202(1):61-67.
106. Mafee MF, Karimi A, Shah J, Rapoport M, Ansari SA. Anatomy and pathology of the eye: role of MR imaging and CT. *Neuroimaging Clin N Am*. Feb 2005;15(1):23-47.

- 1
2
3
4
5
6
7
8
9
10
11
12
13
14
15
16
17
18
19
20
21
22
23
24
25
26
27
28
29
30
31
32
33
34
35
36
37
38
39
40
41
42
43
44
45
46
47
48
49
50
51
52
53
54
55
56
57
58
59
60
- 107.** Mafee MF. Ocular manifestations of cat-scratch disease: role of MR imaging. *AJNR Am J Neuroradiol.* 2005 Jun-Jul 2005;26(6):1303-1304.
- 108.** Ferreira TA, Grech Fonk L, Jaarsma-Coes MG, van Haren GGR, Marinkovic M, Beenakker JM. MRI of Uveal Melanoma. *Cancers (Basel).* Mar 17 2019;11(3).
- 109.** Yiannakas MC, Toosy AT, Raftopoulos RE, Kapoor R, Miller DH, Wheeler-Kingshott CA. MRI acquisition and analysis protocol for in vivo intraorbital optic nerve segmentation at 3T. *Invest Ophthalmol Vis Sci.* Jun 21 2013;54(6):4235-4240.
- 110.** Razek AA, Elkhamary S, Mousa A. Differentiation between benign and malignant orbital tumors at 3-T diffusion MR-imaging. *Neuroradiology.* Jul 2011;53(7):517-522.
- 111.** Bolacchi F, Garaci FG, Martucci A, et al. Differences between proximal versus distal intraorbital optic nerve diffusion tensor magnetic resonance imaging properties in glaucoma patients. *Invest Ophthalmol Vis Sci.* Jun 28 2012;53(7):4191-4196.
- 112.** Niendorf T, Paul K, Graessl A, et al. [Ophthalmological imaging with ultrahigh field magnetic resonance tomography: technical innovations and frontier applications]. *Klin Monbl Augenheilkd.* Dec 2014;231(12):1187-1195.
- 113.** Krueger PC, Stachs O, Hadlich S, et al. MR Microscopy of the human eye at 7.1 T and correlation with histopathology-proof of principle. *Orbit.* Dec 2012;31(6):390-393.
- 114.** Stahnke T, Hadlich S, Wree A, Guthoff RF, Stachs O, Langner S. [Magnetic Resonance Microscopy of the Accommodative Apparatus]. *Klin Monbl Augenheilkd.* Dec 2016;233(12):1320-1323.
- 115.** Falke K, Krüger P, Hosten N, et al. Experimental differentiation of intraocular masses using ultrahigh-field magnetic resonance imaging--a case series. *PLoS One.* 2013;8(12):e81284.
- 116.** de Jong MC, de Graaf P, Pouwels PJW, et al. 9.4T and 17.6T MRI of Retinoblastoma: Ex Vivo evaluation of microstructural anatomy and disease extent compared with histopathology. *J Magn Reson Imaging.* Jun 2018;47(6):1487-1497.
- 117.** Lindner T, Langner S, Falke K, et al. Anatomic and pathological characterization of choroidal melanoma using multimodal imaging: what is practical, what is needed? *Melanoma Res.* Jun 2015;25(3):252-258.
- 118.** Mafee MF, Peyman GA, Peace JH, Cohen SB, Mitchell MW. Magnetic resonance imaging in the evaluation and differentiation of uveal melanoma. *Ophthalmology.* Apr 1987;94(4):341-348.

- 1
2
3
4
5
6
7
8
9
10
11
12
13
14
15
16
17
18
19
20
21
22
23
24
25
26
27
28
29
30
31
32
33
34
35
36
37
38
39
40
41
42
43
44
45
46
47
48
49
50
51
52
53
54
55
56
57
58
59
60
- 119.** de Graaf P, Goricke S, Rodjan F, et al. Guidelines for imaging retinoblastoma: imaging principles and MRI standardization. *Pediatr Radiol*. Jan 2012;42(1):2-14.
- 120.** Franceschiello B, Di Sopra L, Minier A, et al. 3-Dimensional magnetic resonance imaging of the freely moving human eye. *Prog Neurobiol*. Jul 9 2020:101885.
- 121.** Goitein M, Miller T. Planning proton therapy of the eye. *Med Phys*. May-Jun 1983;10(3):275-283.
- 122.** Singh KD, Logan NS, Gilmartin B. Three-dimensional modeling of the human eye based on magnetic resonance imaging. *Invest Ophthalmol Vis Sci*. Jun 2006;47(6):2272-2279.
- 123.** Gorthi S, Duay V, Bresson X, et al. Active deformation fields: dense deformation field estimation for atlas-based segmentation using the active contour framework. *Med Image Anal*. Dec 2011;15(6):787-800.
- 124.** Cootes TF, Taylor CJ, Cooper DH, Graham J. Active Shape Models - Their Training and Application. *Computer Vision and Image Understanding*. Jan 1995;61(1):38-59.
- 125.** Ruegsegger MB, Cuadra MB, Pica A, et al. Statistical Modeling of the Eye for Multimodal Treatment Planning for External Beam Radiation Therapy of Intraocular Tumors. *International Journal of Radiation Oncology Biology Physics*. Nov 15 2012;84(4):E541-E547.
- 126.** Ciller C, De Zanet SI, Ruegsegger MB, et al. Automatic Segmentation of the Eye in 3D Magnetic Resonance Imaging: A Novel Statistical Shape Model for Treatment Planning of Retinoblastoma. *International Journal of Radiation Oncology Biology Physics*. Jul 15 2015;92(4):794-802.
- 127.** De Zanet SI, Ciller C, Rudolph T, et al. Landmark detection for fusion of fundus and MRI toward a patient-specific multimodal eye model. *IEEE Trans Biomed Eng*. Feb 2015;62(2):532-540.
- 128.** Nguyen HG, Pica A, Maeder P, et al. Ocular Structures Segmentation from Multi-sequences MRI Using 3D Unet with Fully Connected CRFs. *Computational Pathology and Ophthalmic Medical Image Analysis*. 2018;11039:167-175.
- 129.** Nguyen HG, Sznitman R, Maeder P, et al. Personalized Anatomic Eye Model From T1-Weighted Volume Interpolated Gradient Echo Magnetic Resonance Imaging of Patients With Uveal Melanoma. *Int J Radiat Oncol Biol Phys*. Nov 15 2018;102(4):813-820.
- 130.** Su Y, Xu X, Zuo P, et al. Value of MR-based radiomics in differentiating uveal melanoma from other intraocular masses in adults. *Eur J Radiol*. Oct 2020;131:109268.

- 1
2
3
4
5
6
7
8
9
10
11
12
13
14
15
16
17
18
19
20
21
22
23
24
25
26
27
28
29
30
31
32
33
34
35
36
37
38
39
40
41
42
43
44
45
46
47
48
49
50
51
52
53
54
55
56
57
58
59
60
- 131.** Mitchell T. *Machine Learning*: Mcgraw-Hill Higher Education; 1995.
- 132.** Tong Y, Lu W, Yu Y, Shen Y. Application of machine learning in ophthalmic imaging modalities. *Eye Vis (Lond)*. 2020;7:22.
- 133.** Ciller C, De Zanet S, Kamnitsas K, et al. Multi-channel MRI segmentation of eye structures and tumors using patient-specific features. *PLoS One*. 2017;12(3):e0173900.
- 134.** de Graaf P, Nguyen HG, de Bloeme C, et al. Automated segmentation of eye structures and retinoblastoma on MRI using Unet with statistical shape priors. Paper presented at: European Congress of Radiology (ECR)2019; Vienna, Austria.
- 135.** Beenakker JWM, Hassan MK, Shamonin D, et al. Automated analysis of uveal melanoma MR-images for an improved treatment determination. *Acta Ophthalmologica*. Mar 2018;96:48-48.
- 136.** Nguyen HG, Pica A, Hrbacek J, et al. A novel segmentation framework for uveal melanoma in magnetic resonance imaging based on class activation maps. *Proceedings of Machine Learning Research*. 2019(102):10.
- 137.** Aerts HJ, Velazquez ER, Leijenaar RT, et al. Decoding tumour phenotype by noninvasive imaging using a quantitative radiomics approach. *Nat Commun*. Jun 3 2014;5:4006.
- 138.** Jansen RW, de Jong MC, Kooi IE, et al. MR Imaging Features of Retinoblastoma: Association with Gene Expression Profiles. *Radiology*. Aug 2018;288(2):506-515.
- 139.** Hrbacek J, Mishra KK, Kacperek A, et al. Practice Patterns Analysis of Ocular Proton Therapy Centers: The International OPTIC Survey. *Int J Radiat Oncol Biol Phys*. May 1 2016;95(1):336-343.
- 140.** Via R, Hennings F, Pica A, et al. Potential and pitfalls of 1.5T MRI imaging for target volume definition in ocular proton therapy. *Radiother Oncol*. Sep 3 2020;154:53-59.
- 141.** Menze BH, Jakab A, Bauer S, et al. The Multimodal Brain Tumor Image Segmentation Benchmark (BRATS). *IEEE Trans Med Imaging*. Oct 2015;34(10):1993-2024.
- 142.** Commowick O, Istace A, Kain M, et al. Objective Evaluation of Multiple Sclerosis Lesion Segmentation using a Data Management and Processing Infrastructure. *Sci Rep*. Sep 12 2018;8(1):13650.
- 143.** Richdale K, Wassenaar P, Teal Bluestein K, et al. 7 Tesla MR imaging of the human eye in vivo. *J Magn Reson Imaging*. Nov 2009;30(5):924-932.

- 1
2
3
4
5
6
7
8
9
10
11
12
13
14
15
16
17
18
19
20
21
22
23
24
25
26
27
28
29
30
31
32
33
34
35
36
37
38
39
40
41
42
43
44
45
46
47
48
49
50
51
52
53
54
55
56
57
58
59
60
- 144.** Minalga E, Rose J, Choi SE, et al. A 20-channel coil for improved magnetic resonance imaging of the optic nerve. *Concepts Magn Reson Part B Magn Reson Eng.* Feb 25 2011;39B(1):26-36.
- 145.** Beenakker JM, Shamonin DP, Webb AG, Luyten GPM, Stoel BC. Automated retinal topographic maps measured with MRI. *Investigative Ophthalmology and Visual Science (IOVS).* 2014; in press.
- 146.** Lindner T, Langner S, Falke K, et al. Anatomic and pathological characterization of choroidal melanoma using multimodal imaging: what is practical, what is needed? *Melanoma Res.* Mar 31 2015.
- 147.** Phal PM, Steward C, Nichols AD, et al. Assessment of Optic Pathway Structure and Function in Patients With Compression of the Optic Chiasm: A Correlation With Optical Coherence Tomography. *Invest Ophthalmol Vis Sci.* Jul 1 2016;57(8):3884-3890.
- 148.** Wezel J, Garpebring A, Webb AG, van Osch MJP, Beenakker JM. Automated eye blink detection and correction method for clinical MR eye imaging. *Magn Reson Med.* Jul 2017;78(1):165-171.
- 149.** Fanea L. Reference 3T MRI parameters of the normal human eye. *Phys Med.* Mar 2018;47:50-57.
- 150.** Wenz D, Kuehne A, Huelnhagen T, et al. Millimeter spatial resolution in vivo sodium MRI of the human eye at 7 T using a dedicated radiofrequency transceiver array. *Magn Reson Med.* Aug 2018;80(2):672-684.
- 151.** Beenakker JM, Wezel J, Groen J, Webb AG, Bornert P. Silent volumetric multi-contrast 7 Tesla MRI of ocular tumors using Zero Echo Time imaging. *PLoS One.* 2019;14(9):e0222573.
- 152.** Koolstra K, Beenakker JM, Koken P, Webb A, Bornert P. Cartesian MR fingerprinting in the eye at 7T using compressed sensing and matrix completion-based reconstructions. *Magn Reson Med.* Apr 2019;81(4):2551-2565.
- 153.** Erb-Eigner K, Willerding G, Taupitz M, Hamm B, Asbach P. Diffusion-Weighted Imaging of Ocular Melanoma. *Investigative Radiology.* 2013;48(10):702-707.
- 154.** Beenakker JW, van Rijn GA, Luyten GP, Webb AG. High-resolution MRI of uveal melanoma using a microcoil phased array at 7 T. *NMR Biomed.* Dec 2013;26(12):1864-1869.
- 155.** Christoforidis JB, Wassenaar PA, Christoforidis GA, Ho VY, Knopp MV, Schmalbrock PM. Retrobulbar vasculature using 7-T magnetic resonance imaging with dedicated eye surface coil. *Graefes Arch Clin Exp Ophthalmol.* Jan 2013;251(1):271-277.

- 1
2
3
4
5
6
7
8
9
10
11
12
13
14
15
16
17
18
19
20
21
22
23
24
25
26
27
28
29
30
31
32
33
34
35
36
37
38
39
40
41
42
43
44
45
46
47
48
49
50
51
52
53
54
55
56
57
58
59
60
- 156.** Fan Q, Nummenmaa A, Witzel T, et al. Investigating the capability to resolve complex white matter structures with high b-value diffusion magnetic resonance imaging on the MGH-USC Connectom scanner. *Brain Connect.* Nov 2014;4(9):718-726.
- 157.** Fan Q, Witzel T, Nummenmaa A, et al. MGH-USC Human Connectome Project datasets with ultra-high b-value diffusion MRI. *Neuroimage.* Jan 1 2016;124(Pt B):1108-1114.
- 158.** Siemens-Healthineers. 2020; Siemens 3T Vida Brochure. Available at: https://static.healthcare.siemens.com/siemens_hwem-hwem_sxxa_websites-context-root/wcm/idc/groups/public/@global/@imaging/@mri/documents/download/mda5/nzgw/~edis/siemens_healthineers_mr_magnetom_vida-07268000.pdf. Accessed November 14th, 2020.
- 159.** U.S.-Food&Drug-Administration. 2020; https://www.accessdata.fda.gov/cdrh_docs/pdf20/K201615.pdf. Accessed November 22th 2020.
- 160.** Xu X, Wang Y, Hu H, et al. Readout-segmented echo-planar diffusion-weighted imaging in the assessment of orbital tumors: comparison with conventional single-shot echo-planar imaging in image quality and diagnostic performance. *Acta Radiologica.* Jan 01 2017:284185117695667.
- 161.** de Graaf P, Pouwels PJ, Rodjan F, et al. Single-shot turbo spin-echo diffusion-weighted imaging for retinoblastoma: initial experience. *AJNR Am J Neuroradiol.* Jan 2012;33(1):110-118.
- 162.** Heinrichs U, Utting JF, Frauenrath T, et al. Myocardial T2* mapping free of distortion using susceptibility-weighted fast spin-echo imaging: a feasibility study at 1.5 T and 3.0 T. *Magn Reson Med.* Sep 2009;62(3):822-828.
- 163.** Niendorf T. On the application of susceptibility-weighted ultra-fast low-angle RARE experiments in functional MR imaging. *Magn Reson Med.* Jun 1999;41(6):1189-1198.
- 164.** Hillenbrand C, Hahn D, Haase A, Jakob P. MR CAT scan: a modular approach for hybrid imaging. *Magnetic Resonance Materials in Physics, Biology and Medicine.* 2000/10/01 2000;10(3):183-199.
- 165.** Berg I, Palmowski-Wolfe A, Schwenzler-Zimmerer K, et al. Near-real time oculodynamic MRI: a feasibility study for evaluation of diplopia in comparison with clinical testing. *Eur Radiol.* Feb 2012;22(2):358-363.

- 1
2
3
4
5
6
7
8
9
10
11
12
13
14
15
16
17
18
19
20
21
22
23
24
25
26
27
28
29
30
31
32
33
34
35
36
37
38
39
40
41
42
43
44
45
46
47
48
49
50
51
52
53
54
55
56
57
58
59
60
- 166.** Sengupta S, Smith DS, Smith AK, Welch EB, Smith SA. Dynamic Imaging of the Eye, Optic Nerve, and Extraocular Muscles With Golden Angle Radial MRI. *Invest Ophthalmol Vis Sci*. Aug 1 2017;58(10):4390-4398.
- 167.** van Rijn GA, Mourik JE, Teeuwisse WM, Luyten GP, Webb AG. Magnetic resonance compatibility of intraocular lenses measured at 7 Tesla. *Invest Ophthalmol Vis Sci*. Jun 8 2012;53(7):3449-3453.
- 168.** Winter L, Oberacker E, Ozerdem C, et al. On the RF heating of coronary stents at 7.0 Tesla MRI. *Magn Reson Med*. Oct 2015;74(4):spcone.
- 169.** Santoro D, Winter L, Muller A, et al. Detailing radio frequency heating induced by coronary stents: a 7.0 Tesla magnetic resonance study. *PLoS One*. 2012;7(11):e49963.
- 170.** Kraff O, Wrede KH, Schoemberg T, et al. MR safety assessment of potential RF heating from cranial fixation plates at 7 T. *Med Phys*. Apr 2013;40(4):042302.
- 171.** Winter L, Seifert F, Zilberti L, Murbach M, Ittermann B. MRI-Related Heating of Implants and Devices: A Review. *J Magn Reson Imaging*. May 26 2020.
- 172.** Niendorf T, Schulz-Menger J, Paul K, Huelnhagen T, Ferrari VA, Hodge R. High Field Cardiac Magnetic Resonance Imaging: A Case for Ultrahigh Field Cardiac Magnetic Resonance. *Circ Cardiovasc Imaging*. Jun 2017;10(6).
- 173.** Nouredine Y, Kraff O, Ladd ME, et al. Radiofrequency induced heating around aneurysm clips using a generic birdcage head coil at 7 Tesla under consideration of the minimum distance to decouple multiple aneurysm clips. *Magn Reson Med*. Nov 2019;82(5):1859-1875.
- 174.** Culo B, Valencerina S, Law M, Shellock FG. Assessment of metallic patient support devices and other items at 7-Tesla: Findings applied to 46 additional devices. *Magn Reson Imaging*. Apr 2019;57:250-253.
- 175.** Kraff O, Quick HH. 7T: Physics, safety, and potential clinical applications. *J Magn Reson Imaging*. Dec 2017;46(6):1573-1589.
- 176.** Chen B, Schoemberg T, Kraff O, et al. Cranial fixation plates in cerebral magnetic resonance imaging: a 3 and 7 Tesla in vivo image quality study. *MAGMA*. Jun 2016;29(3):389-398.
- 177.** Niendorf T, Frydman L, Neeman M, Seeliger E. Google maps for tissues: Multiscale imaging of biological systems and disease. *Acta Physiol (Oxf)*. Feb 2020;228(2):e13392.

- 1
2
3
4
5
6
7
8
9
10
11
12
13
14
15
16
17
18
19
20
21
22
23
24
25
26
27
28
29
30
31
32
33
34
35
36
37
38
39
40
41
42
43
44
45
46
47
48
49
50
51
52
53
54
55
56
57
58
59
60
- 178.** Walter U, Niendorf T, Graessl A, et al. Ultrahigh field magnetic resonance and colour Doppler real-time fusion imaging of the orbit--a hybrid tool for assessment of choroidal melanoma. *Eur Radiol.* May 2014;24(5):1112-1117.
- 179.** Flogel U, Schluter A, Jacoby C, et al. Multimodal assessment of orbital immune cell infiltration and tissue remodeling during development of graves disease by (1) H(19) F MRI. *Magn Reson Med.* Aug 2018;80(2):711-718.
- 180.** Ji Y, Waiczies H, Winter L, et al. Eight-channel transceiver RF coil array tailored for (1) H/(19) F MR of the human knee and fluorinated drugs at 7.0 T. *NMR Biomed.* Jun 2015;28(6):726-737.
- 181.** Nagel AM, Umathum R, Rosler MB, et al. (39) K and (23) Na relaxation times and MRI of rat head at 21.1 T. *NMR Biomed.* Jun 2016;29(6):759-766.
- 182.** Wenz D, Nagel AM, Lott J, Kuehne A, Niesporek SC, Niendorf T. In vivo potassium MRI of the human heart. *Magn Reson Med.* Jan 2020;83(1):203-213.
- 183.** He X, Erturk MA, Grant A, et al. First in-vivo human imaging at 10.5T: Imaging the body at 447 MHz. *Magn Reson Med.* Jul 2020;84(1):289-303.
- 184.** Sadeghi-Tarakameh A, DelaBarre L, Lagore RL, et al. In vivo human head MRI at 10.5T: A radiofrequency safety study and preliminary imaging results. *Magn Reson Med.* Jul 2020;84(1):484-496.
- 185.** Winter L, Niendorf T. Electrodynamics and radiofrequency antenna concepts for human magnetic resonance at 23.5 T (1 GHz) and beyond. *MAGMA.* Jun 2016;29(3):641-656.
- 186.** Winter L, Ozerdem C, Hoffmann W, et al. Design and evaluation of a hybrid radiofrequency applicator for magnetic resonance imaging and rf induced hyperthermia: electromagnetic field simulations up to 14.0 Tesla and proof-of-concept at 7.0 Tesla. *PLoS One.* 2013;8(4):e61661.
- 187.** Budinger TF, Bird MD, Frydman L, et al. Toward 20 T magnetic resonance for human brain studies: opportunities for discovery and neuroscience rationale. *MAGMA.* Jun 2016;29(3):617-639.
- 188.** Polenova T, Budinger TF. Ultrahigh field NMR and MRI: Science at a crossroads. Report on a jointly-funded NSF, NIH and DOE workshop, held on November 12-13, 2015 in Bethesda, Maryland, USA. *J Magn Reson.* May 2016;266:81-86.

- 1
2
3 **189.** Behr VC, Weber T, Neuberger T, et al. High-resolution MR imaging of the rat spinal cord in
4 vivo in a wide-bore magnet at 17.6 Tesla. *MAGMA*. Dec 2004;17(3-6):353-358.
5
6
7 **190.** Stroh A, Faber C, Neuberger T, et al. In vivo detection limits of magnetically labeled
8 embryonic stem cells in the rat brain using high-field (17.6 T) magnetic resonance imaging.
9 *Neuroimage*. Feb 1 2005;24(3):635-645.
10
11
12 **191.** Steinbrecher A, Weber T, Neuberger T, et al. Experimental autoimmune encephalomyelitis in
13 the rat spinal cord: lesion detection with high-resolution MR microscopy at 17.6 T. *AJNR Am*
14 *J Neuroradiol*. Jan 2005;26(1):19-25.
15
16
17
18 **192.** Herold V, Morchel P, Faber C, Rommel E, Haase A, Jakob PM. In vivo quantitative three-
19 dimensional motion mapping of the murine myocardium with PC-MRI at 17.6 T. *Magn Reson*
20 *Med*. May 2006;55(5):1058-1064.
21
22
23
24 **193.** Weiss K, Melkus G, Jakob PM, Faber C. Quantitative in vivo ¹H spectroscopic imaging of
25 metabolites in the early postnatal mouse brain at 17.6 T. *MAGMA*. Feb 2009;22(1):53-62.
26
27
28 **194.** Raya JG, Melkus G, Adam-Neumair S, et al. Diffusion-tensor imaging of human articular
29 cartilage specimens with early signs of cartilage damage. *Radiology*. Mar 2013;266(3):831-
30 841.
31
32
33
34 **195.** Winter P, Andelovic K, Kampf T, et al. Fast self-navigated wall shear stress measurements in
35 the murine aortic arch using radial 4D-phase contrast cardiovascular magnetic resonance at
36 17.6 T. *J Cardiovasc Magn Reson*. Oct 14 2019;21(1):64.
37
38
39 **196.** Waiczies S, Rosenberg JT, Kuehne A, et al. Fluorine-19 MRI at 21.1 T: enhanced spin-lattice
40 relaxation of perfluoro-15-crown-5-ether and sensitivity as demonstrated in ex vivo murine
41 neuroinflammation. *MAGMA*. Feb 2019;32(1):37-49.
42
43
44 **197.** Schepkin VD, Neubauer A, Nagel AM, Budinger TF. Comparison of potassium and sodium
45 binding in vivo and in agarose samples using TQTPPI pulse sequence. *J Magn Reson*. Apr
46 2017;277:162-168.
47
48
49 **198.** Schepkin VD. Sodium MRI of glioma in animal models at ultrahigh magnetic fields. *NMR*
50 *Biomed*. Feb 2016;29(2):175-186.
51
52
53 **199.** Schepkin VD, Bejarano FC, Morgan T, Gower-Winter S, Ozambela M, Jr., Levenson CW. In
54 vivo magnetic resonance imaging of sodium and diffusion in rat glioma at 21.1 T. *Magn*
55 *Reson Med*. Apr 2012;67(4):1159-1166.
56
57
58
59
60

- 1
2
3 **200.** Schepkin VD, Elumalai M, Kitchen JA, Qian C, Gor'kov PL, Brey WW. In vivo chlorine and
4 sodium MRI of rat brain at 21.1 T. *MAGMA*. Feb 2014;27(1):63-70.
5
6
7 **201.** Schepkin VD, Brey WW, Gor'kov PL, Grant SC. Initial in vivo rodent sodium and proton MR
8 imaging at 21.1 T. *Magn Reson Imaging*. Apr 2010;28(3):400-407.
9
10
11 **202.** Shemesh N, Rosenberg JT, Dumez JN, Grant SC, Frydman L. Distinguishing neuronal from
12 astrocytic subcellular microstructures using in vivo Double Diffusion Encoded 1H MRS at 21.1
13 T. *PLoS One*. 2017;12(10):e0185232.
14
15
16 **203.** Leftin A, Rosenberg JT, Solomon E, Calixto Bejarano F, Grant SC, Frydman L. Ultrafast in vivo
17 diffusion imaging of stroke at 21.1 T by spatiotemporal encoding. *Magn Reson Med*. Apr
18 2015;73(4):1483-1489.
19
20
21
22 **204.** Rosenberg JT, Shemesh N, Muniz JA, Dumez JN, Frydman L, Grant SC. Transverse relaxation
23 of selectively excited metabolites in stroke at 21.1 T. *Magn Reson Med*. Feb 2017;77(2):520-
24 528.
25
26
27 **205.** Roussel T, Rosenberg JT, Grant SC, Frydman L. Brain investigations of rodent disease models
28 by chemical exchange saturation transfer at 21.1 T. *NMR Biomed*. Nov 2018;31(11):e3995.
29
30
31 **206.** Ciller C. *Multi-modal imaging in ophthalmology: image processing methods for improving*
32 *intra-ocular tumor treatment via MRI and Fundus image photography* [PhD thesis].
33 Lausanne: Faculté de biologie et médecine, Université de Lausanne; 2017.
34
35
36
37
38
39
40
41
42
43
44
45
46
47
48
49
50
51
52
53
54
55
56
57
58
59
60

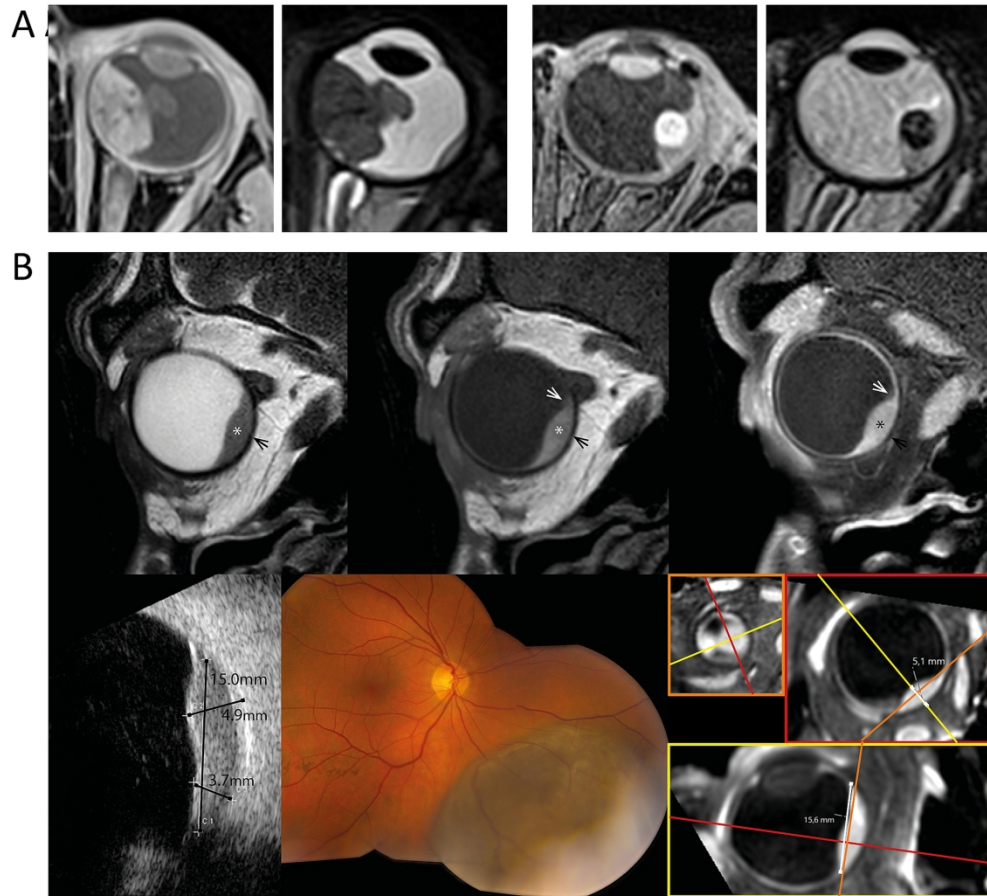


Figure 1

201x182mm (600 x 600 DPI)

1
2
3
4
5
6
7
8
9
10
11
12
13
14
15
16
17
18
19
20
21
22
23
24
25
26
27
28
29
30
31
32
33
34
35
36
37
38
39
40
41
42
43
44
45
46
47
48
49
50
51
52
53
54
55
56
57
58
59
60

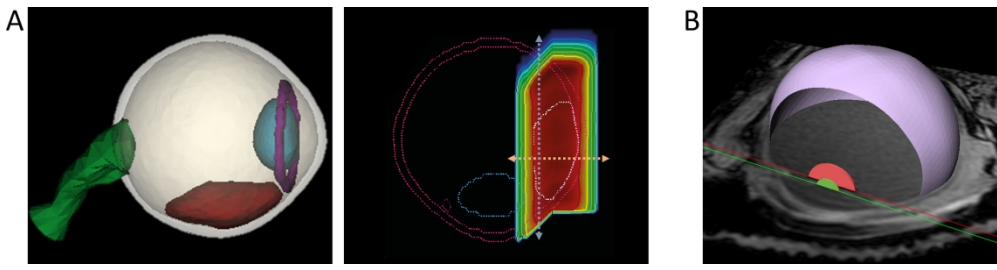


Figure 2

267x68mm (600 x 600 DPI)

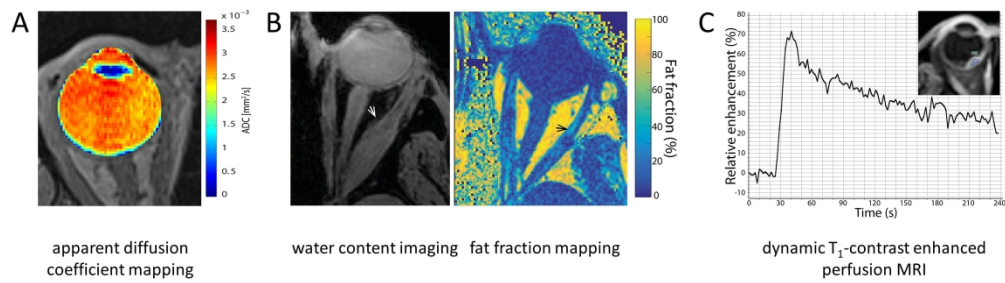


Figure 3

199x55mm (600 x 600 DPI)

1
2
3
4
5
6
7
8
9
10
11
12
13
14
15
16
17
18
19
20
21
22
23
24
25
26
27
28
29
30
31
32
33
34
35
36
37
38
39
40
41
42
43
44
45
46
47
48
49
50
51
52
53
54
55
56
57
58
59
60

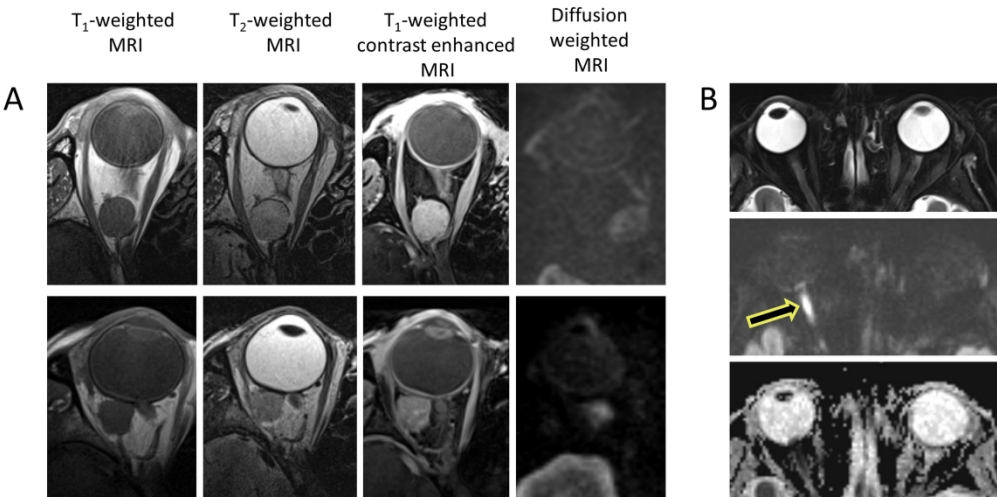


Figure 4

236x117mm (600 x 600 DPI)

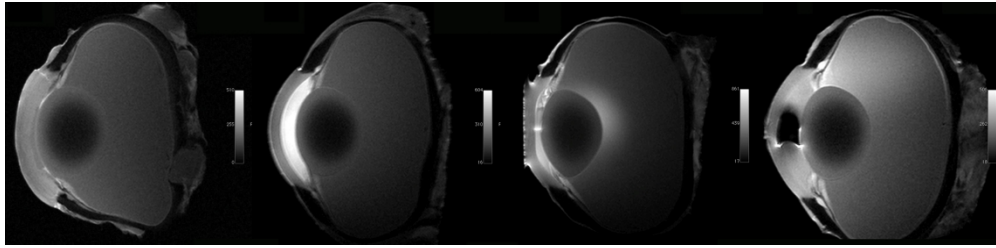


Figure 5

248x60mm (600 x 600 DPI)

1
2
3
4
5
6
7
8
9
10
11
12
13
14
15
16
17
18
19
20
21
22
23
24
25
26
27
28
29
30
31
32
33
34
35
36
37
38
39
40
41
42
43
44
45
46
47
48
49
50
51
52
53
54
55
56
57
58
59
60

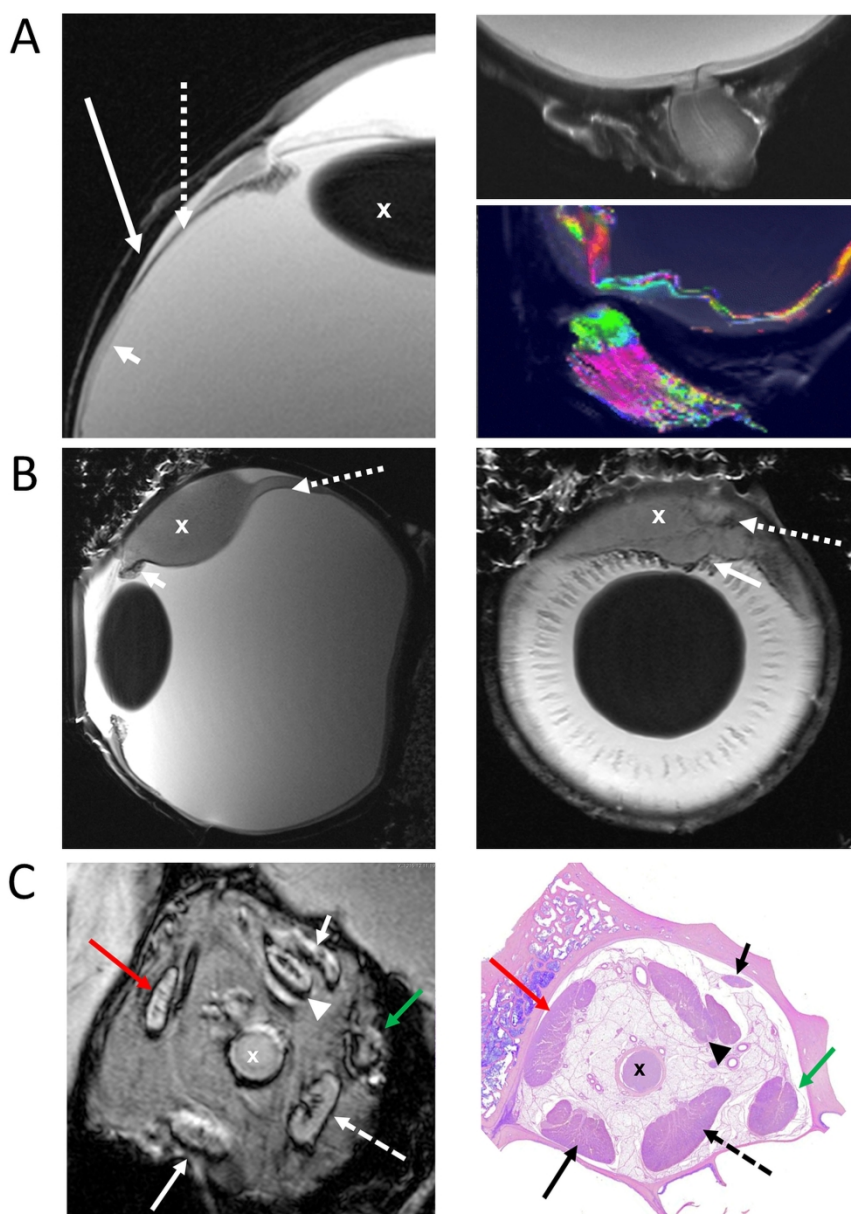


Figure 6

132x186mm (600 x 600 DPI)

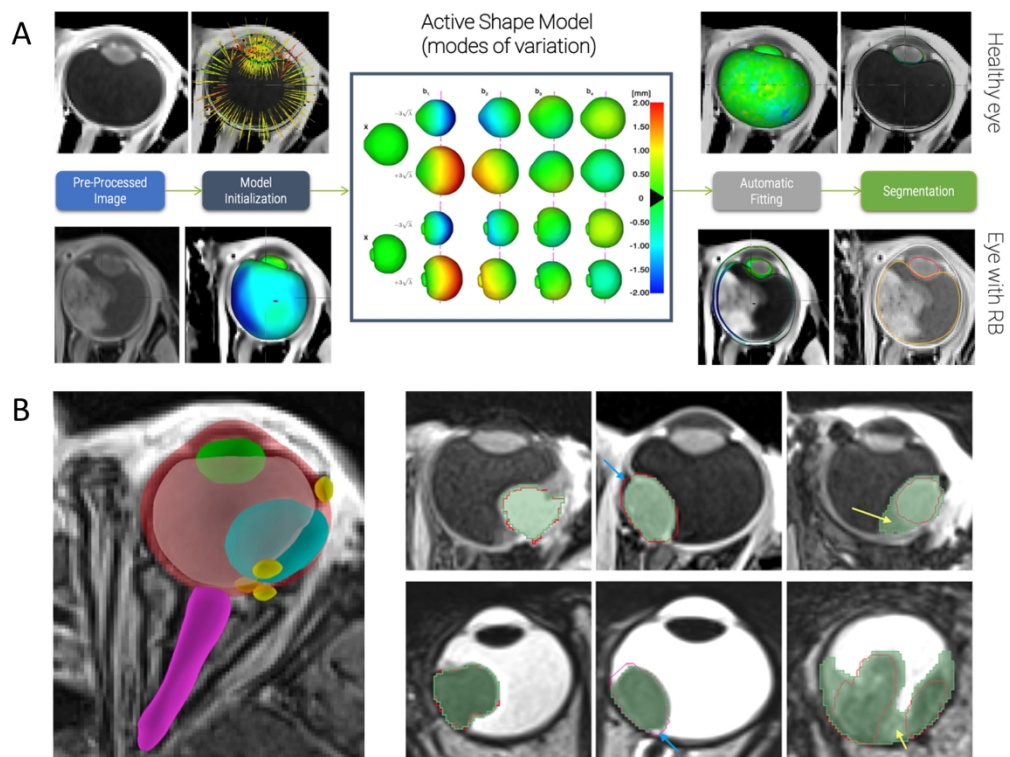


Figure 7

239x180mm (600 x 600 DPI)

1
2
3
4
5
6
7
8
9
10
11
12
13
14
15
16
17
18
19
20
21
22
23
24
25
26
27
28
29
30
31
32
33
34
35
36
37
38
39
40
41
42
43
44
45
46
47
48
49
50
51
52
53
54
55
56
57
58
59
60



Figure 8

269x78mm (600 x 600 DPI)

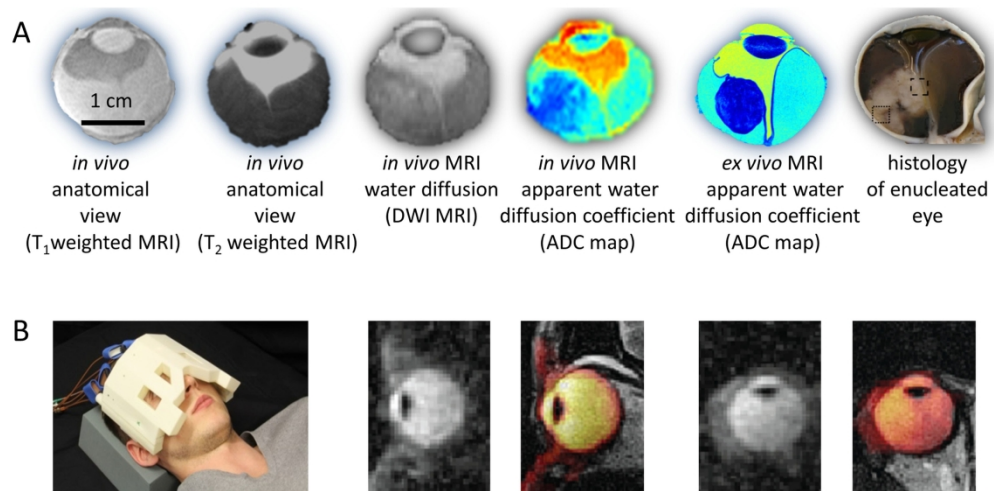


Figure 9

259x128mm (600 x 600 DPI)